DEVELOPMENT OF SU-8 AND PDMS MINIATURED BOATS AND FLOTILLAS

by

HAO LI

Presented to the Faculty of the Graduate School of

The University of Texas at Arlington in Partial Fulfillment

of the Requirements

for the Degree of

DOCTOR OF PHILOSOPHY

THE UNIVERSITY OF TEXAS AT ARLINGTON

August 2010

ACKNOWLEDGEMENTS

I would like to thank my committee chair, Professor Jung-Chih Chiao, who has expressed deep concern on my research work and helped me greatly on my dissertation preparation and graduation schedule; I would highly appreciate his encouragement and advice when these were most needed.

I would like to express the deepest appreciation to my committee member and research advisor, Professor Cheng Luo, who has the attitude and the substance of a genius: he continually and convincingly conveyed a spirit of adventure in regard to research and scholarship, and an excitement in regard to teaching. Without his guidance and persistent help this dissertation would not have been possible.

I would like to thank my committee members, Professor Donald Butler, Professor Samir Iqbal and Dr. Hung Chang, whose work demonstrated to me that concern for global affairs supported by an “engagement” in comparative literature and modern technology should always transcend academia and provide a quest for our times.

In addition, I would like to thank my colleagues, Dr. Xinchuan Liu, Dr. Anirban Chakraborty, Mr. Lei Qiao and Mr. Hui Wang for their help with my research.

Financial support was provided by the University of Texas, Arlington, and NSF Grant NSF-ECS-0529104.

July 15, 2010

ABSTRACT

DEVELOPMENT OF SU-8 AND PDMS MINIATURED
BOATS AND FLOTILLAS

Hao Li, PhD.

The University of Texas at Arlington, 2010

Supervising Professor: Cheng Luo

In this work, we developed miniaturized SU-8 and PDMS miniaturized boats and flotillas, and explored their design, fabrication, actuation, motions and driving mechanisms. Like large-scale boats and flotillas, these miniaturized boat and flotillas can be potentially applied to transport designed targets to desired locations in small fluidic systems. These may also be employed as mixers, rotators and so on.

We first develop an SU-8 boat, and studied its design, fabrication, actuation and motions. In three types of tests conducted o water free surfaces of different heights in a 30 cm long channel, the microboat had a speed on the order of 0.1 m/s, and propulsive forces ranged from 159 to 250 μN. It took 1 to 2 s for the boat to go through the channel, and resistance coefficients varied from 0.144 to 0.324. Also, when the resistance coefficient was 0.324, the boat was still able to travel a distance of 91.4 cm within 5.33 s.

We then initiated the effort of developing miniaturized SU-8 and PDMS flotillas, which were capable of moving on a water surface. We explored their designs, fabrication, propulsion, and motions in straight and circular channels. The SU-8 flotilla comprised five miniaturized SU-8 boats connected with a Nylon rope, and was fabricated using ultra-violet lithographic techniques. The PDMS flotilla comprised five miniaturized PDMS boats connected with PDMS lines, and was fabricated using molding techniques.

Both types of flotillas were actuated due to the difference between fore-and-aft surface tensions. The SU-8 flotilla was tested in three straight and one circular channels at water levels of 3 mm, 6 mm and 9 mm, respectively. In all the tests, the flotilla moved like a rigid object, and no collisions were observed between neighboring boats. Travel distances were above 0.44 m, and average speeds varied from 40.2 mm/s to 103.2 mm/s. Both the travel distances and the average speeds were found to increase with the increasing water depth and channel width. The two ends of the microtrain had direct contact with the outer sidewall of the circular channel during a circular motion. The support forces of the outer sidewall at these contact points provided the centripetal force needed for the circular motion. The same tests were conducted for the PDMS flotilla, and the corresponding testing results were similar to those of the SU-8 flotilla. Compared with a single boat, such a flotilla can be potentially employed to transport a large amount of supply in small fluidic applications.

Finally, we explored the driving mechanisms of the developed boats and flotillas. A floating solid fragment may have a spontaneous motion on a water surface when a liquid, which has a surface tension lower than water, exits the solid fragment and has contact with water. This motion may be induced due to the surface tension difference between water and the liquid. In order to interpret this motion, it is important to know how the liquid exits the solid fragment. We reported in-situ observation of exchange processes of water and isopropyl alcohol (boat propellant) inside both close and open reservoirs of cm-scaled PDMS boats. Based on this observation and force analysis, we interpreted driving mechanisms of these boats. We found that the exchange processes may be different in the PDMS boats of respective close and open reservoirs. The PDMS boat of a close reservoir may have a bubble trapped in its reservoir. This bubble slowed down the exiting process of the IPA from the reservoir, made the motion last longer, and enabled the boat to have a longer travel distance. Also, such a boat might have gurgling-like motions (i.e., approximately periodic motions of speeding up and slowing down) after the majority of the isopropyl alcohol had exited the reservoir. On the other hand, neither bubbles and nor gurgling-like phenomena were found during the motions of the PDMS boat with an open reservoir.

Financial support for this project was provided by the University of Texas, Arlington, and NSF Grant NSF-ECS-0529104.

TABLE OF CONTENTS

LIST OF ILLUSTRATIONS

CHAPTER 1

INTRODUCTION

1.1 Background

Similar to what macro-boats are used in daily life, miniaturized boats and flotillas can be potentially employed to transport target of interest from one place to another for small-scale fluidic applications. A macro-flotilla consists of a group of macro-boats; it is capable of delivering large amount of various materials. However, as will be addressed in Chapter 2, miniaturized boats and flotillas have not been extensively studied, despite the fact that much research has been done on movable micro-systems on solid surface or in air, such as comb drives [1], micro-motors [2], and micro-flies [3]. Therefore, in this work, we developed miniaturized boats and flotillas, and explored their design, fabrication, actuation and motion in small channels.

1.2 Statement of problem

We have chosen SU-8 and PDMS as building material to fabricate our miniaturized boats and flotillas. The SU-8 photoresist is a negative tone epoxy-based resist initially developed by IBM [4]. It was designed for the microfabrication of high aspect-ratio micro-components for micro-electro-mechanical systems (MEMS). Due to its properties: high sensitivity, high resolution, low optical absorption, high thermal stability and good chemical resistance, SU-8 is widely used in various applications, such as structures or supports for microstructures and basic material for molding or packaging [5,6]. We chose SU-8 mainly because of three reasons: 1) it is compatible with UV lithography technique, through which precise size and shape control can be obtained. 2) it can be used to fabricate multi-layered structures [7-9], which is essential for the realization of our design. 3) its density (1190kg/m^3) is slightly higher than water [10], which guarantees that when a boat/flotilla is placed in water, the

generated surface tension between boat/flotilla body and water surface could overcome its weight and make the boat/flotilla afloat.

PDMS is a silicone elastomer with desirable properties that makes it attractive for the development of MEMS and micro-fluidics components for biomedical applications [11-13]. It is chemically inert, thermally stable, permeable to gases, and simple to handle/manipulate; it exhibits isotropic and homogeneous properties, incurs lower cost than silicon, and can conform to submicron features for development of microstructures [14, 15]. PDMS is also favorable due to its density (970kg/m^3) [16] and molding property [17-19]. With an appropriate mold (made of SU-8 in our case), PDMS gels can be cast and cured such that a comparatively complicated structure could be fabricated as a whole piece. This would make it potentially desirable for batch production if necessary.

Like macro-boats and macro-flotillas, for the purpose of material delivery and transportation, miniaturized boats and flotillas should exhibit high mobility, be able to change directions, and capable of stopping at desired locations. Furthermore, due to their small dimensions, conventional techniques for manufacturing macro-boats and macro-flotillas may not be suited to fabricate these miniaturized boats and flotillas. Therefore, the following four problems should be solved in order to properly develop these miniaturized vehicles.

1.2.1 How to fabricate miniaturized boats and flotillas?

Due to small dimensions of miniaturized boats, the conventional manufacturing techniques are not suited for their fabrication. Instead, micro-fabrication techniques are uniquely suited for producing such small items. The most important function of a boat is to transport a target from one place to another; therefore, the mobility of the boat is the major concern. Although the design of macro-boat shapes (for reduction of water resistance) applies to miniaturized boats and flotillas, the means of propelling a miniaturized boat and flotilla cannot be borrowed from a macro-boat. It involves much effort and time to generate complicated systems, such as propellers,

using micro-fabrication techniques. Consequently, other propulsive approaches should be adopted for generating miniaturized boats and flotillas that avoid the necessity of those complicated systems.

1.2.2 How to propel and stop miniaturized boats and flotillas?

Surface tension is an effect within the surface layer of a liquid. It causes the liquid surface layer to behave like an elastic sheet. It allows insect, such as a water strider, to walk on water. It also allows small items, such as a sewing needle, to float on water surface. Surface tension acts tangentially to the interface between a boat and water, pointing towards the outside of the boat.

Surface tension gradient may induce the movement of a liquid droplet on the surface of another liquid. For example, when a drop of alcohol is released in water, water rushes away from the dropping location and a hollow spot is created. Since water has a higher surface tension than alcohol, more watery portion draws itself away from the more alcoholic portion, as interpreted by Thomson [20]. Surface tension gradient may also cause the movement of a floating solid fragment on a liquid surface. These surface tension-driven motions of liquids and solid fragments are caused by the so-called Marangoni effect, which is the mass transfer along an interface due to surface tension gradient.

We applied the Marangoni effect [21] based driving method in this project. The Marangoni effect is the reason that surface tension gradients around a floating solid fragment could cause the fragment's movement on a liquid surface. This effect can therefore be used as a propulsion mechanism instead of motor based propulsion. Unlike a micro-motor, which is comparatively complex in fabrication and application, thereby making it inappropriate to work on miniaturized boats and flotillas; the Marangoni effect based propulsion does not need to install complex hardware on miniaturized boats and flotillas, thus offering a suitable alternative for similar applications. Accordingly, the advantage is that this effect could not only largely reduce

the complexity in both fabrication and application, but also offer a feasible solution to the actuation of our miniaturized boats and flotillas.

On some occasions, it is desirable to stop the miniaturized boats and flotillas, such as the case after they reach the desired location while carrying a sensor. Therefore we also need to address the method that can successfully stop the miniaturized boats and flotillas if necessary.

1.2.3 What design to adopt?

In order to carry more cargos through a channel, a long boat is desired so that more storage space would be available. Such a long boat would be able to travel in a straight channel, but it may not be able to move in a curved channel due to its incapability of making turns. On the other hand, we observe that although a macro-train is much longer and has more storage space than a macro-truck, it is still able to have radial motion on a curved track. This is due to the fact that the macro-train is bendable owing to its interconnecting pins. Inspired by the design of macro-trains and based on the work of the miniaturized boat, we also initiated the effort of developing a so-called miniaturized flotilla in this work for transportation of large amount of various materials.

1.2.4 How to test miniaturized boats and flotillas?

We tested miniaturized boats in straight channels, and miniaturized flotillas in both straight and circular channels. We used a SONY HDR 200 camcorder to record their motions so they can be analyzed subsequently.

In addition to the capability of traveling in a small fluidic channel, for the purpose of material delivery and sensing, a miniaturized boat or flotilla also needs to stop at a desired place. Furthermore, it is necessary to collect a miniaturized boat or flotilla after each application for multiple uses [22]. Therefore, in this work, these two issues are explored as well. They will be resolved with the use of magnetic forces and inclined surfaces, respectively.

1.3 Delimitations and Limitations

Despite their advantages, the developed miniaturized boats and flotillas actuated by organic solvent still have limitations, as listed below:

We focus on miniaturized boats and flotillas that move on water surface, propelled by force induced through the Marangoni effect. However, there exists occasions where underwater transfer of cargo is necessary.

Our experiments are mainly carried out in open channels, which have top openings. This type of channels facilitate the tests and analysis, but under certain situations it is desirable to make them move in enclosed channels.

Some delimitation that exists regarding the miniaturized boat and flotilla's actuation by organic solvent is due to the following reasons:

1) The propulsion mechanism of the boats is surface tension based Marangoni effect, which makes it inappropriate to work underwater. Furthermore, the material from which the boats and flotillas are made is either SU-8 or PDMS; their density is merely slightly larger than that of water, so the boats' and flotillas' weight is not large enough to overcome the surface tension.

2) In our test, open channel has some desirable features. First, it allows us to observe and record the boats' and flotillas' movement conveniently. If the channels are enclosed, even if the channel top was sealed by a transparency, it would obstruct the view and video quality of the recorded movement.

After we demonstrated the feasibility of miniaturized boats and flotillas acting as a sensor delivery method in a comparatively macro scale, we continued to reduce the dimension of the miniaturized boats and flotillas by adopting other types of SU-8, e.g. SU-8 50, 20, and 5, instead of SU-8 100. These other types of SU-8 are capable of building smaller structures, which can achieve sizes as small as 10 micrometer. With the dimensions reduced, the corresponding develop time would be considerably less; so we could extend this time appropriately to allow complete development in the chambers (fuel, cargo) on board, which requires longer develop

time due to insufficient contact between the developer and inner chamber walls. For example, we can observe from the figure below that the SU-8 developer can reach the SU-8 photoresist freely from the above or sideways, and it can flow easily too, all these largely guarantees sufficient contact between the Su-8 and its developer, therefore providing maximum develop efficiently. However, as the development progresses and chambers form, the amount of developer that can get access to the inside of the chamber becomes less, and the mobility of these developers reduces too. Both of these factors obstruct further adequate development inside the chamber. Therefore, prolonged time is necessary for complete development of the chamber area.

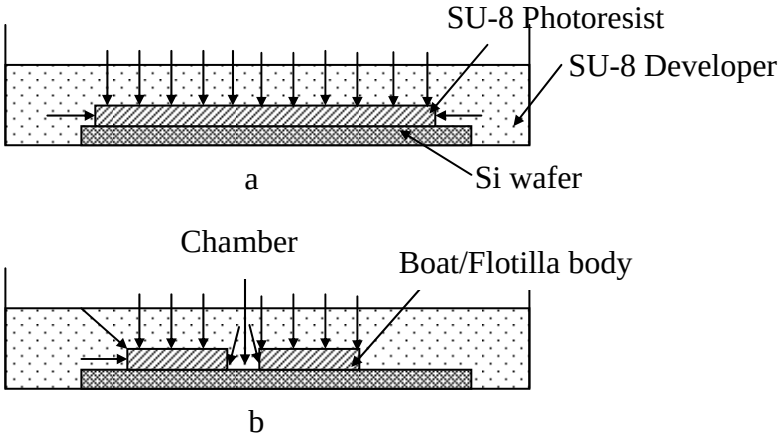

Figure 1.1 Schematic of the development process of SU-8 photoresist at (a) the beginning of the development. (b) the end of the development.

CHAPTER 2

LITERATURE REVIEW

2.1 Introduction

Micro-robot is an application that employs surface tension and various propulsive methods have been explored for its actuation. Recently many micro-robots have been developed for various purposes due to advantages of the precise process technology. In the medical field and in industry application, a new type of fish-like microrobot that can swim smoothly in water or aqueous medium has been urgently demanded [24-25]. Meanwhile, several types of fish-like microrobot using SMA actuator, GMA actuator, PZT actuator and polymer actuator have been reported so far [26-31]. In the past two decades, miniaturized robots that are able to move on the water surface (strider robot), as well as underwater (underwater robot) have also received much attention.

2.2 Related Research

2.2.1 Underwater Robots

Propulsion and steering of a floating mini-robot based on thermal Marangoni flow is proposed [32]. Fig. 2.1-(a) shows a schematic of the legged mini-robot. Fig. 2.1-(b) shows the enlarged view of the cross section of the leg on the water surface and lift forces acting on it. Depicted in Fig. 2.1-(c) is an enlarged view of the leg of the mini-robot showing the location of the heater.

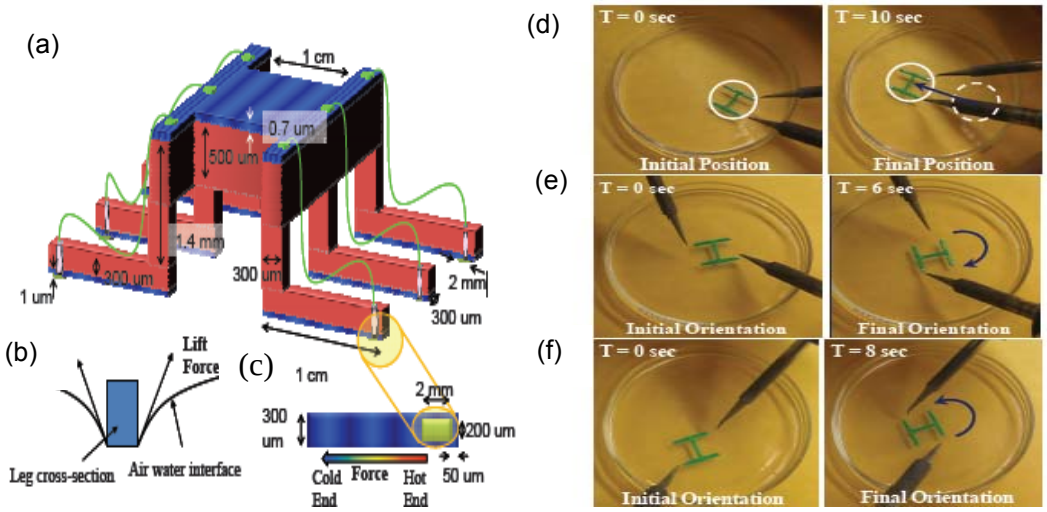

Figure 2.1 (a) Schematic of the six legged mini-robot. (b) Enlarged view of the cross section of the leg showing the water surface and lift forces acting on it (c) Enlarged view of the leg of the mini-robot showing the location of the heater. Preliminary experiments suggest the feasibility of (d) translational, (e) clockwise and (f) anti-clockwise motion of the proposed robot [32].

Preliminary experiments were conducted by spot heating the liquid in the dish with a soldering iron. Fig. 2.1-(d) shows a sequence of an H shaped model making translational movement; Fig. 2.1-(e) clockwise rotational movement and Fig. 2.1-(f) counterclockwise rotational movement.

A miniature robot was proposed [33] that mimic the structure of a water strider; its schematics and motion sequence were shown below. Fig. 2.2-(b) displays a CAD model of the water strider robot. Fig. 2.2-(c) shows a robot making translational motion at speed=3cm /s. Fig. 2.2-(d) shows a robot making rotational movement (right turn) at speed=0.5 rad /s.

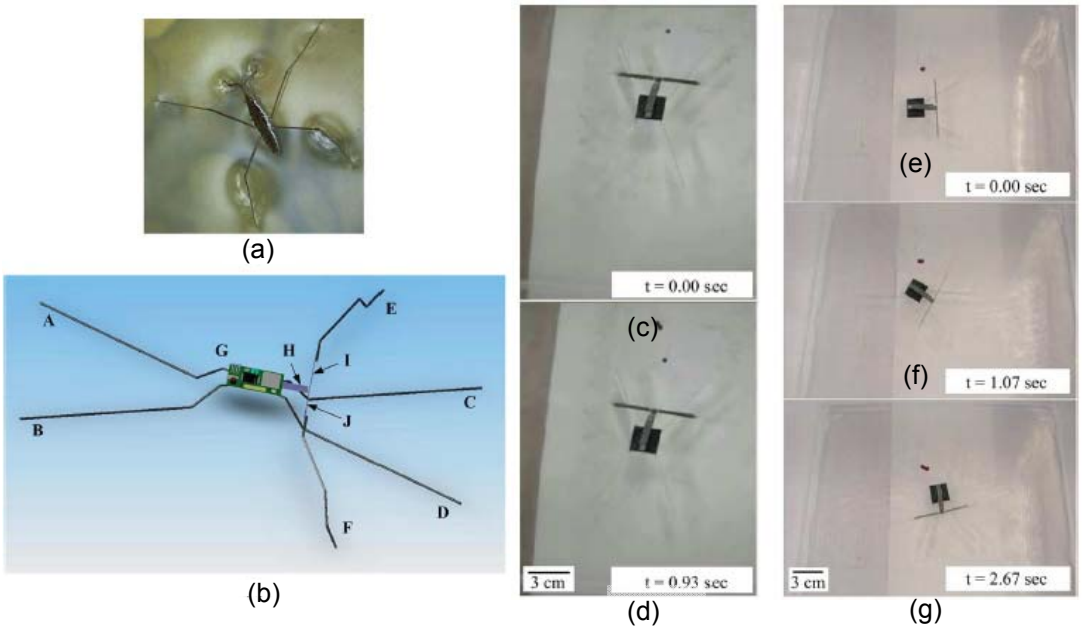

Figure 2.2 (a) Photo of an insect water strider. (b) Conceptual CAD model of the water strider robot. A, B, C, and D: the supporting legs; E and F: the actuating legs; G: the body with on-board electronics and power source; H: the middle actuator; I and J: the right and left actuators, respectively. (c) - (g), snapshots of the different motions of the robot on the surface of water. (c),(d)- Forward motion of 3 cm/s (e)-(g) Right turn of 0.5 rad/s [33].

Several underwater robots are also devised, such as micro biped robot shown in Fig. 2.3 [34].

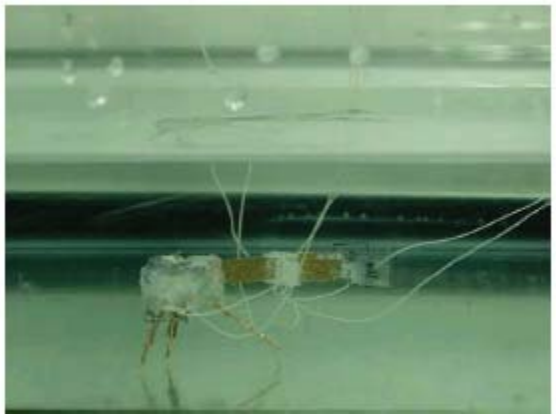

Figure 2.3 Walking underwater robot [34]

Miniaturized boats and flotillas have been shown to be a viable modality in its ease of sterilization, possible high drug entrapment, production of large batch sizes and long circulation

half-life of vesicles. First, polymers like SU-8 and PDMS can be sterilized with UV radiation/sterilization and ethanol rinsing, which is unlikely for processing liposomes. The manufacturing method, which is highly UV-lithography focused, provides potential of mass-production, as we have seen in modern microchips industry. Moreover, the comparatively solid structure of SU-8/PDMS guarantees its durability within necessary time frame.

In the past 15 years, the Marangoni effect has been applied to driving gels, whose dimensions ranged from millimeter to centimeter scales [35-38].

2.2.2 Centimeter Scale Plastic Object

A plastic object was first put in water and organic solvents, e.g. ethanol, was dropped at different locations beside it through a syringe. This would result it to make translational (Fig 2.4(a)-(d), a sequence was shown at its 0, 6^{th}, 9^{th} and 12^{th} second) or rotational (Fig 2.4(e)-(h), a sequence was shown at its 0, 6^{th}, 12^{th} and 18^{th} second) movement [39].

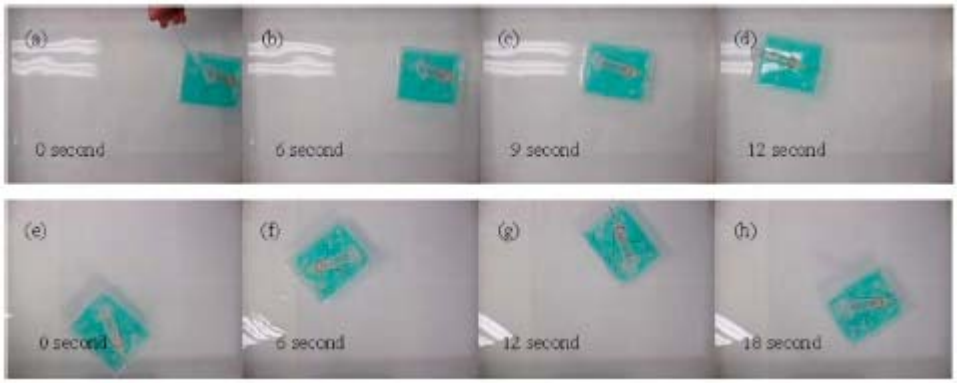

Figure 2.4 Dropping ethanol into water generates the motion of a plastic boat floating on water. By changing the relative position of ethanol dropping location, the movement direction can be steered [(a)-(d)] in a straight line, or [(e)-(h)] in a circular track [39].

The movement types are controlled by changing the relative position where the ethanol would be dropped- centered position (to obtain translational movement), or off-centered position (to obtain rotational movement).

2.2.3 Centimeter Scale Gel

It is further discovered that by immersing a gel into a liquid which has a lower surface tension than water, like ethanol, the gel would be soaked with this liquid like sponge absorbing water [35].

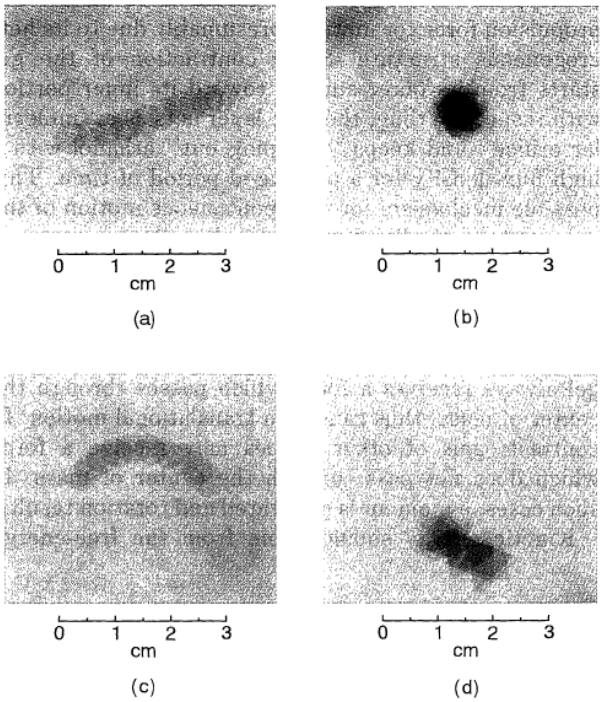

Figure 2.5 Gels of various shapes in motion (a) Translational motion of a disk-shaped gel (b) rotational motion of a square gel; c) and d) motions composed of translational and rotational by (c) a disk and (d) a triangular rod [35].

Once this gel was removed from the liquid and put into water, the absorbed liquid would be expulsed into surrounding water in all directions. The resulting surface tension difference between water and the liquid would make the gel make either translational or rotational motion.

It is found that gel shape has much influence on its movement. Several shapes were developed and put into test, as shown in the above pictures. Fig. 2.5(a) is a disk shaped gel 0making translational movement. Fig. 2.5(b) -a square making rotational movement. Fig. 2.5(c) -

a disk making both translational and rotational motions and Fig. 2.5(d) -similar movement made by a triangular rod.

The same group then explored its driving mechanism. The hydrophobic alkyl chains of the gel impart to the surface perm-selective properties, whereby an organic solvent from inside the gel can be ejected out into the water, but water from outside cannot permeate into the gel. The surface of the gel released the swelling solvent and was rendered crystalline soon after it came into contact with water, while the interior responded more slowly. This process set up an osmotic as well as a hydrostatic pressure across the crystalline, perm-selective skin that allowed a gradual ejection of the organic solvent and resulted in prolonged motion of the gel. When the symmetry in solvent release was accentuated by covering all but the rear end of the gel, a more directed and prolonged motion was observed. In summary, by spreading water-soluble organic solvent in the gel to water surface, there is osmotic and hydrostatic pressures generated in the gel, which keep pumping the solvents away from the gel into the water, therefore generating surface tension gradient around the gel, which can produce driving force for the gel's motion [36].

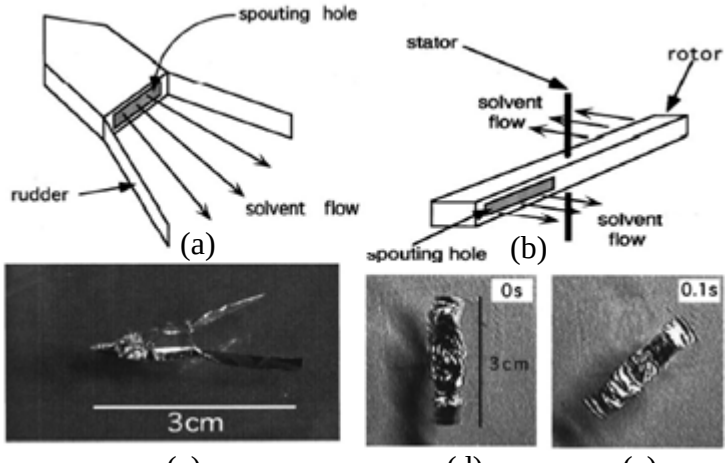

Figure 2.6 Illustration of schematic of the polymer showing (a) translational motion and (b) rotational motion. [36]. Photographs of the polymer gel showing (c) translational motion and (d), (e) rotational motion.

These researchers in Japan continued to contrive certain configurations, whose schematic illustrations are shown in Fig 2.6(a)-(b). They consisted of a body and a reservoir. The

reservoir was used to store the organic solvent. When the solvent exits from the outlet, a surface tension gradient was created to propel the gel [37].

The body of these structures was made of gel, but wrapped in aluminum foil for the ease of demonstration. These foils are also essential in deciding the moving directions of the gels- they determine the opening or outlet through which the solvents exit, as indicated by the arrows in the schematics; the generated propulsion force, which is in the opposite direction to the solvent's exit direction, would determine the gels movement- speed and direction. If there were no aluminum foil, the solvent would expulse in all directions, thus making it hard to control the gel's movement. Fig. 2.6(c) shows a boat shaped gel making translational movement. Fig. 2.6(d) and Fig. 2.6(e) showed a rotational sequence at 0 and 0.1 second. It was further employed to construct a generator, which was able to produce a voltage as high as 15 mV for over 30 minutes.

2.2.4 Millimeter Scale Gel

The gels in previous research are fabricated manually, thereby making it hard to control its shape precisely; in another research at John Hopkins, UV lithography method was used to fabricate gels with better size and shape control [38].

Four types of shapes were fabricated. Fig. 2.7(a) showed a translational movement sequence at time 0, 0.133 and 0.283 s. Fig. 2.7(b) - a trapezoidal gel that was able to make rotational motion, the sequence shown in the pictures was taken at time 0, 0.067 and 0.133 s, with angular velocity of 235 rpm. Fig. 2.7(c) - an oval gel was able to make rotational motion with angular speed of 900 rpm. Fig. 2.7(d) - a symmetric Y shaped gel was able to generate rotational motion with spinning speed at 1400rpm.

From these pictures we see that the shape and size of the gel have a considerable influence to both the type and speed of the gel's movement.

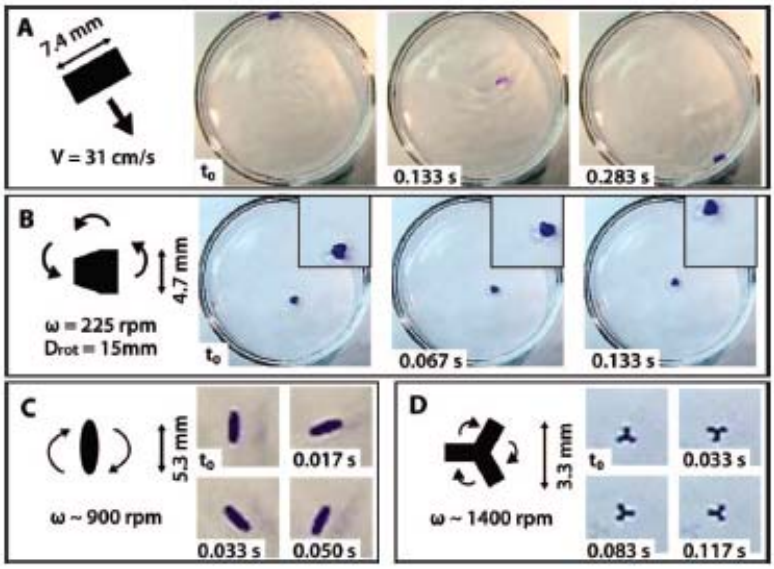

Figure 2.7 Different motions observed with photo-patterned PNIPAm gels of different shapes. (A) 2:1 rectangular gel (convex) shape translating in a straight line (B) A trapezoidal (convex) shape with aspect ratio of 1:1 processing (C) A 3:1 oval (convex) shape spinning (D) A symmetric Y (concave) shape spinning [38].

2.3 Conclusions of Literature Review

The research mentioned above all have their advantages, but some limitations still remain: 1) The shapes of gels could not be well-defined. Even the UV lithography based method cannot obtain a desirable shape because the gel swells under the UV light exposure; not to mention other manual fabrication methods. 2) The propellant exits the gel from all directions during the propulsion. The only way to control their movement is by fabricating gels of various shapes, which could hardly meet requirement of advanced applications.

Therefore, other propulsion methods are needed, and we developed boats and flotillas of well-defined shapes and well-controlled propulsion, such that their motions can be rationally controlled.

During our experiment, a so-called squat and trim phenomenon was observed, mainly induced by the surface tension difference between water and isopropyl alcohol (IPA), which is propellant in our case. This phenomenon is related to the miniaturized boats' movement in the

vertical, rather than horizontal direction. The induced difference in surface tension gradient created a hollow spot behind the stern, which in turn made the boat sink and tilt along the sidewall of the hollow spot.

CHAPTER 3

METHODOLOGY

3.1 Introduction

In this section first we try to address the questions raised in section 1.2 -"State of problem". The answers will be arranged in three parts- questions related to 1) miniaturized SU-8 boat, 2) miniaturized SU-8 flotilla and 3) miniaturized PDMS flotilla. Finally we will summarize and discuss our future work.

3.2 Miniaturized SU-8 boat

3.2.1 Fabrication

3.2.1.1 Fabrication of an SU-8 Miniaturized Boats

We can conclude from discussions in Chapter 2 that gel shape is essential in determining its movement; but previously mentioned methods cannot generate satisfactory results. One promising field is UV lithography based fabrication, which requires material that does not swell when exposed under UV light. We therefore choose SU-8 since it has been proved to be able to endure prolonged UV exposure without losing its physical and chemical stability.

The fabrication of an SU-8 miniaturized boat includes three steps:

(i) Fig. 3.1(a) - place a transparency on an S1813 photoresist coated silicon wafer, spin-coat the first SU-8 layer on the transparency, and pattern the SU-8 to form the bottom layer of the boat using the UV lithography approach. This layer would define the body of the miniaturized boat.

(ii) Fig. 3.1(b) - spin-coat the second SU-8 layer on top of the first one, which would define reservoirs and nozzles in the miniaturized boat. This step also requires the use of the UV lithography technique,

(iii) Fig. 3.1-(c) - dissolved S1813 using acetone and remove the transparency, together with the generated SU-8 miniaturized boats, from the silicon wafer.

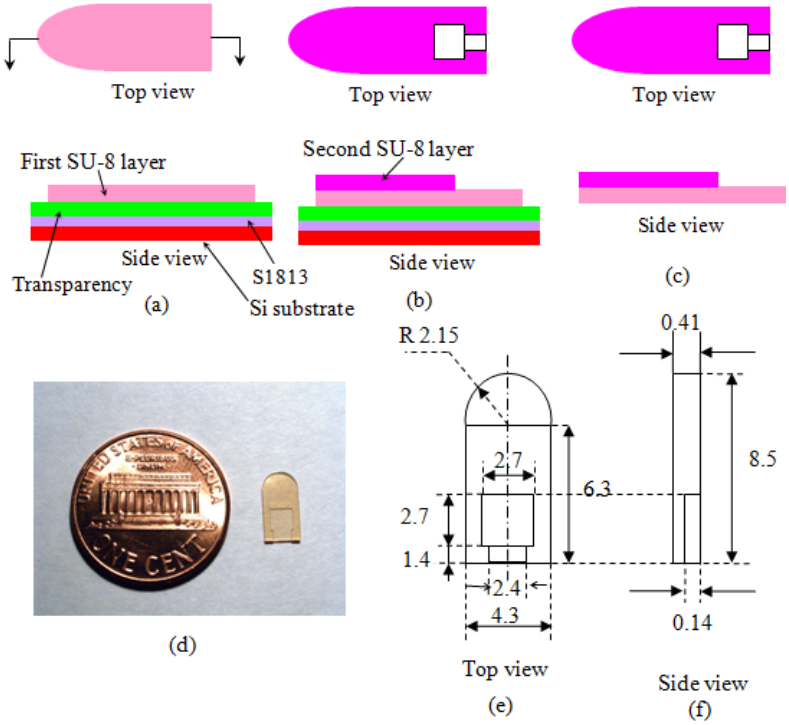

Figure 3.1 Three-step fabrication procedure: (a) bond a transparency on an S1813-coated 4-inch silicon wafer, and pattern the first SU-8 layer on the transparency using the standard ultra-violet lithography approach, (b) pattern the second SU-8 layer, and (c) dissolve S1813 using acetone and remove the transparency, together with the generated SU-8 miniaturized boats from the silicon wafer. (d) a representative miniaturized boat generated, and (e) and (f) its dimensions (unit: mm).

Two masks were used in the fabrication while patterning the two SU-8 layers. In the final step, the SU-8 miniaturized boats were released from the substrate using a new method that our group recently developed. The transparency had a circular shape with a diameter of 4.5 inch, which was a little wider than a 4-inch Si wafer for ease of grabbing the edge of the transparency and subsequent peeling off from the substrate. The transparency was stable

during the entire fabrication process, i.e., no damages were observed visually during its exposure to employed chemicals like acetone, S1813, SU-8, and SU-8 developer. This transparency was cut out of a normal transparent film frequently used for slides presentation. The intermediate S1813 layer between the transparency and the substrate was not exposed under UV light, as it would normally do, but served as the adhesion layer to make the transparency bond closely with the Si wafer. It also served as the UV light adsorption layer, and good SU-8 patterns were generated accordingly. When transparency was directly placed on the Si substrate, air gaps generally formed between the transparency and the Si wafer, which would reflect random UV light from the Si wafer to the SU-8 layer during exposure, generating poor patterns. The transparency, together with the SU-8 boat, were released from the Si substrate via etch of S1813 with acetone. After that, the SU-8 miniaturized boats could be easily separated from the underlying transparency even manually.

3.2.1.2 Fabrication of magnetic SU-8 miniaturized boats

We also wanted to test the stoppage of miniaturized boats in a channel; this included incline stoppage and magnetic stoppage. The later is the reason for our fabrication of magnetic SU-8 miniaturized boat.

The bottom SU-8 layer of a miniaturized boat was embedded with hard magnetic micro-particles, i.e., hard barium ferrite (NdFeB) particles, which would interact with a magnetic microstructure made from NdFeB on the bottom of a water filled micro-channel or small open area, thereby stopping the miniaturized boat at a position right above the microstructure. A micro-device can be actuated by piezoelectric [40], thermal [41-42], electrostatic [43-46], and magneto-static forces [47-48]. Magneto-static forces were used to stop miniaturized boats due to the simplicity in applying this method with no other external devices. Hard permanent magnetic material with high remnant magnetic moment was adopted since they require a lower power level while activating a device, as compared to soft magnetic materials. NdFeB micro-

particles (UltraFine Powder Technology) has been demonstrated to be a suitable material with a relatively high remnant magnetic moment of 8.1×10^{-5} A.m^2, which implies high magnetostatic forces, compared with other magnetic materials such as Ba ferrite micro-particles [49]. Therefore, it was employed as a material for both the composite film and magnetic microstructure. The composite permanent film was fabricated by mixture of SU-8 and hard magnetic micro-particles.

3.2.2 Propulsion of an SU-8 miniaturized boat

The miniaturized boat was propelled by releasing organic solvent in the boat's fuel chamber, which propelled the boat through the Marangoni effect.

3.3 Miniaturized SU-8 flotilla

3.3.1 Fabrication

Three-step procedure was used to fabricate the designed miniaturized flotillas as follows (Fig. 3.2):

(1) Attach a piece of transparency on a silicon wafer, and define the positions of Nylon wires on the transparency (Fig. 3.2(a)),

(2) Pattern two SU-8 layers into the form of a series of miniaturized boats connected with the Nylon wires (Fig. 3.2(b)-(c)), and

(3) Remove the miniaturized flotilla from the substrate (Fig. 3.2(d)).

The first fabrication step included three sub-steps: (i) attach a layer of transparency on a silicon wafer using a layer of a positive photoresist S1813 as the bonding agency, (ii) coat another layer of S1813 on the transparency and generate line marks in this S1813 layer using the UV lithography approach, and (iii) place Nylon wires along the generated S1813 line marks and fix them on the transparency with glue.

The second fabrication step includes two sub-steps: (i) spin-coat a first SU-8 layer on the transparency and pattern the SU-8 to form the bottom layer of the miniaturized flotillas (this layer does not have any structures and served as a platform, on which SU-8 structures will be further built) using the UV lithography approach, and (ii) spin-coat a second SU-8 layer on the first SU-8 film and produce cargo chambers, reservoirs and nozzle of the miniaturized boats in the second SU-8 layer using the UV lithography approach again. In the first sub-step, the first

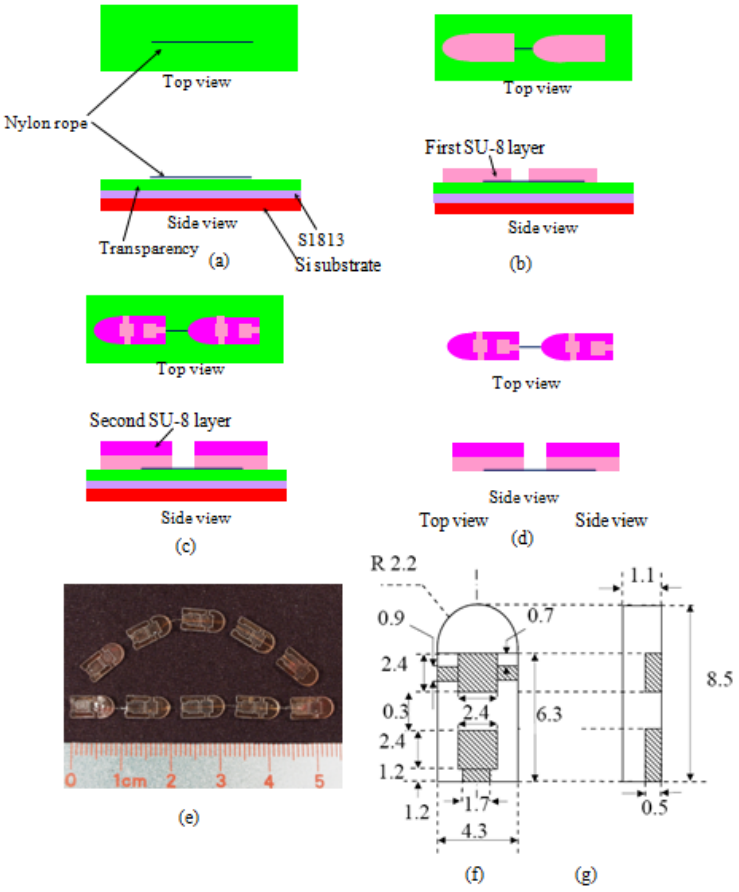

Figure 3.2 Illustration of fabrication procedure: (a) place a transparency on an S1813-coated 4-inch silicon wafer, and place Nylon wires at the defined locations on the transparency, (b) pattern the first SU-8 layer on the transparency using the conventional UV lithography approach, (c) pattern the second SU-8 layer, and (d) dissolve S1813 using acetone and remove the transparency, together with the generated SU-8 miniaturized flotillas, from the silicon wafer. (e) Two representative miniaturized flotillas generated, and (f) and (g) the dimensions of a component miniaturized flotilla in a miniaturized flotilla (unit: mm).

SU-8 layer was patterned on the Nylon wires. Consequently, part of a Nylon wire was embedded into this SU-8 layer, while the rest of the wire was still exposed, linking the miniaturized boats together as a miniaturized flotilla.

In the third step, the SU-8 miniaturized flotillas were released from the substrate using a new method that we have recently developed [57]. The transparency, together with the SU-8 miniaturized flotillas, can be released from the Si substrate via etch of S1813 through acetone. After that, these miniaturized flotillas can be easily separated from the transparency underneath.

One mask was used in the first fabrication step to define the positions of the Nylon wires, while another two were applied in the second fabrication step for patterning the two layers of SU-8 using the UV lithography method. The major part of the fabrication process is similar to what we used for generating a single miniaturized boat [23]. A critical difference is that an additional step (i.e., the first step) had to be included in fabricating a miniaturized flotilla for incorporating a Nylon wire in the miniaturized flotilla to connect individual miniaturized boats.

Two representative miniaturized flotillas generated and their dimensions are given in Fig. 3.2(e)-(g). They had the same dimensions, and each consisted of five identical miniaturized boats. The top layer was 140 μm thick. The reservoir and nozzle of a miniaturized boat had dimensions of 2.7 mm x 2.7 mm x 140 μm and 2.4 mm x 1.4 mm x 140 μm, respectively. The bottom layer was 270 μm thick. The mass of a miniaturized boat was 19.5 mg. The total volume of the reservoir and nozzle was 1.49 μl. The length of the Nylon wire between two neighboring miniaturized boats was 2.7 mm. The total length of the miniaturized flotilla was 55.0 mm. Therefore, the circular channels inside which such a miniaturized flotilla could travel should have perimeters greater than 55.0 mm. That is, these channels should have radii larger than 8.8 mm. As shown in Fig. 3.2(e), one of the miniaturized flotillas was bent to indicate that these miniaturized flotillas were bendable for making radial motion. Such a miniaturized flotilla could be further bent to form a circle with a radius of 8.8 mm, where the first and fifth boats were linked together. This implies that these miniaturized flotillas were flexible enough to travel inside

the smallest channels allowed by their length. The type of miniaturized flotillas shown in Fig. 3.2 (e) was used in the tests.

The difference between fabrication of SU-8 flotilla and SU-8 boat is that nylon wires are employed as connectors between multiple boats, e.g. five boats, in our work.

3.3.2 Propulsion of a miniaturized flotilla

3.3.2.1 Force analysis

The miniaturized flotilla was propelled due to the Marangoni effect. As in the case of a macrotrain, one of the five miniaturized boats in the miniaturized flotilla was chosen as a locomotive, and the other four boats would be used for carrying cargos in practical applications. A simple analysis was given below to determine which miniaturized boat should be actuated so that maximum propulsive force would be generated to propel the miniaturized flotilla. Surface tension acted tangentially to the interface between boat and water, pointing outwards the boat. As shown in Fig. 3.3, let F_1 through F_{10} denote the surface tension around the five miniaturized boats. Set F_w and F_a to be surface tensions of water and IPA, respectively. The resultant force, P, on the miniaturized flotilla induced by the surface tension was: $P=(F_1-F_{10}+F_3-F_2+F_5-F_4+F_7-F_6+F_8-F_9)W$, where W represents the boat width. While the first miniaturized boat served as the locomotive, i.e., IPA was only loaded to the first miniaturized boat, the IPA that exited the rear of the first miniaturized boat only affected the surface tension behind it and before the second miniaturized boat. Therefore, $F_1=F_4=F_5=F_6=F_7=F_8=F_9=F_{10}=F_w$, $F_2=F_a$ and $P=(F_3-F_a)W$. The concentration of the IPA that diffused out of the locomotive nozzle decreased as it exited further away from the nozzle. The corresponding surface tension increased with the decreasing concentration [49-50]. Thus, $F_a< F_3< F_w$, and P provided a propulsive force to drive the miniaturized flotilla forward. Similarly, when the second, third or fourth miniaturized boat was chosen as the locomotive, respectively, the corresponding propulsive force was $P=(F_5-F_a)W$, $P=(F_7-F_a)W$, and $P=(F_9-F_a)W$, where $F_a<F_5<F_w$, $F_a<F_7<F_w$, and $F_a<F_9<F_w$. If the fifth miniaturized

boat was selected as the locomotive, then $F_1=F_2=F_3=F_4=F_5=F_6=F_7=F_8=F_9$, $F_{10}=F_a$ and $P=(F_w-F_a)W$. Obviously, the largest propulsive force would be generated when the fifth miniaturized boat was chosen to be the actuating one. Therefore, this miniaturized boat should be chosen as the locomotive of the miniaturized flotilla.

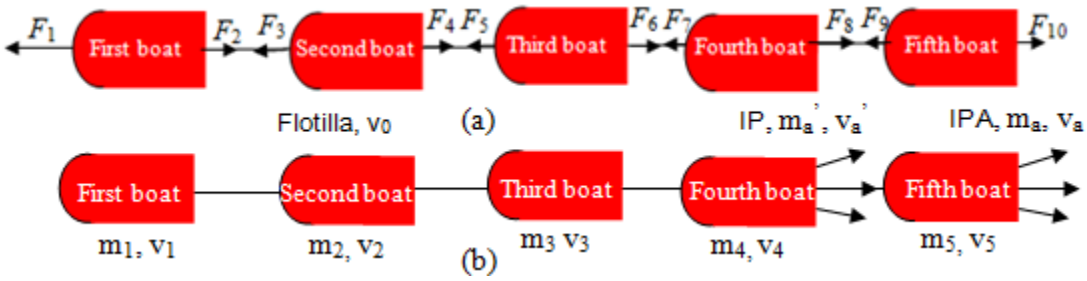

Figure 3.3 (a) Surface tensions in front and behind each miniaturized boat in a straight motion. (b) Illustration for energy analysis of the flotilla.

3.3.2.2 Energy analysis

If we assume the IPA that was released into the fuel chamber of the 5th boat completely exited the chamber in the end at an average speed of v_0, the energy relationship is:

After the release of the IPA into the fuel chamber, the flotilla begins to move. In the end, the total energy that the IPA imparts was used to propel the flotilla as well as to overcome the water resistance. Therefore, we have:

$$\frac{1}{2}m_1\bar{v}_1^2+\frac{1}{2}m_2\bar{v}_2^2+\frac{1}{2}m_3\bar{v}_3^2+\frac{1}{2}m_4\bar{v}_4^2+\frac{1}{2}m_5\bar{v}_5^2+E_w=\frac{1}{2}m_a\bar{v}_a^2$$

Where E_W is the energy consumed by water resistance.

Since each individual boat has similar mass and the same average speed, let

$$m_1=m_2=m_3=m_4=m_5=m_0,\quad \bar{v}_1=\bar{v}_2=\bar{v}_3=\bar{v}_4=\bar{v}_5=\bar{v}_0$$

Then

$$5\left(\frac{1}{2}m_0\bar{v}_0^2\right)+E_w=\frac{1}{2}m_a\bar{v}_a^2$$

If we assume the energy lost to water resistance is much less than the kinetic energy of the boats

$$E_w << \frac{1}{2} m_0 \bar{v}_0^2$$

Then

$$\frac{5}{2} m_0 \bar{v}_0^2 = \frac{1}{2} m_a \bar{v}_a^2 \Rightarrow \bar{v}_0 = \sqrt{\frac{m_a}{5m_0}}\, \bar{v}_a$$

Each time the same amount of IPA was released into the fuel chamber of one of the boats, ma is a constant; therefore, the average speed of the flotilla is determined by the average exit speed of the IPA.

If we consider the case where the 5th and 4th boat are injected with IPA, and the average IPA's exit speed is v_a and v_a'. From the above illustration, we can see that when IPA exits from the 5th boat, there is no encumbrance. However, when exits from the 4th boat, it is obvious that the IPA will meet the 5th boat, which would invariably reduce its speed. Therefore, we have $v_a > v_a'$.

When substitute this result into the equation above, we can obtain

$$\bar{v}_0 > \bar{v}_0'$$

This can qualitatively explain why the flotillas would travel faster when driven by IPA dropped into the 5th boat than the 4th boat.

Similarly, this derivation can be applied to the 1st, 2nd, 3rd boat and explain why their speed is also less as compared to IPA being released into the 5th boat.

3.3.3 Testing Setup

In order to apply a water train, e.g., to transport materials from one place to another, it is important to understand the following four issues: (i) how was the train actuated, (ii) how did it have straight motions, (iii) how did it have radial motions, and (iv) what were travel distance and

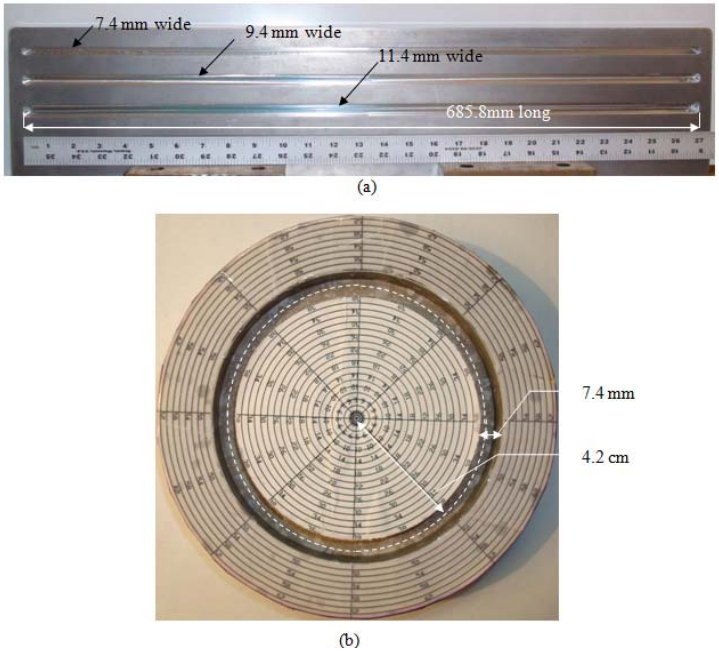

Figure 3.4 (a) three straight and (b) one circular channels used in the tests.

average speed? To address these issues, the fabricated trains were tested in three straight and one circular channel. These two types of channels were both fabricated from steel plates using a CNC milling machine. The three straight channels had the same length and height of 685.8 mm and 10.0 mm, respectively (Fig. 3.4(a)). They differed in the widths, which were 7.4 mm, 9.4 mm and 11.4 mm. For simplicity, they were called the 7-mm channel, 9-mm channel and 11-mm channel, respectively. The circular channel was 10.3 mm deep and 7.4 mm wide. The radius and perimeter of the loop measuring from the middle line of the circular channel were 42 mm and 264 mm, respectively (Fig. 3.4(b)).

Steel and paper rulers were placed beside the straight and circular channels, respectively, to determine the position of a miniaturized flotilla at a particular instant. The

volume of loaded IPA in each test was 90% that of the locomotive reservoir. When the reservoir was fully filled, the IPA might spill out of the reservoir. Therefore, the maximum volume of loaded IPA was chosen to be 90% that of the locomotive reservoir. A miniaturized flotilla was released in a channel after IPA had been filled and spread evenly in the locomotive reservoir using a needle. Its motion was recorded using a camcorder (model: SONY HDR XR500 with 30 frames per second). The video was then played in software Adobe Premier Element to examine the motions.

3.4 Miniaturized PDMS flotilla

3.4.1 Fabrication

A three-step procedure was used to fabricate the designed miniaturized flotillas as follows (Fig. 3.5):

(i) attach a piece of transparency on a silicon wafer (Fig. 3.5(a)).

(ii) pattern two SU-8 layers into the form of a series of miniaturized flotilla molds (Fig. 3.5(b)-(c)), and

(iii) prepare PDMS and pour it into the SU-8 mold, cure and separate it from the mold to obtain PDMS miniaturized flotilla (Fig. 3.5(d)).

In the first fabrication step we attach a layer of transparency on a silicon wafer using a layer of a positive photoresist S1813 as the bonding agency.

The second fabrication step includes two sub-steps: (i) spin-coat a first SU-8 layer on the transparency, pattern the SU-8 to form the first layer of the miniaturized flotilla mold and produce structures that define cargo chamber, reservoir and nozzle for later PDMS trains, using the UV lithography approach, and (ii) spin-coat a second SU-8 layer on the first SU-8 film (this layer did not have any structures but served as a foundation for the later PDMS miniaturized flotilla) using the UV lithography approach again. This step is similar to a previous work [23], the

difference is that both masks used here bear exact reverse pattern because we are generating an SU-8 mold instead of SU-8 miniaturized flotilla.

In the third step, we prepare PDMS by mixing Sylgard polymer base and curing agent with a ratio of 10:1, e.g. 3g base: 0.3g curing agent. After thoroughly mixing them, pour the mixture onto the SU-8 mold, scrape off excess PDMS gel on the mold surface with a razor

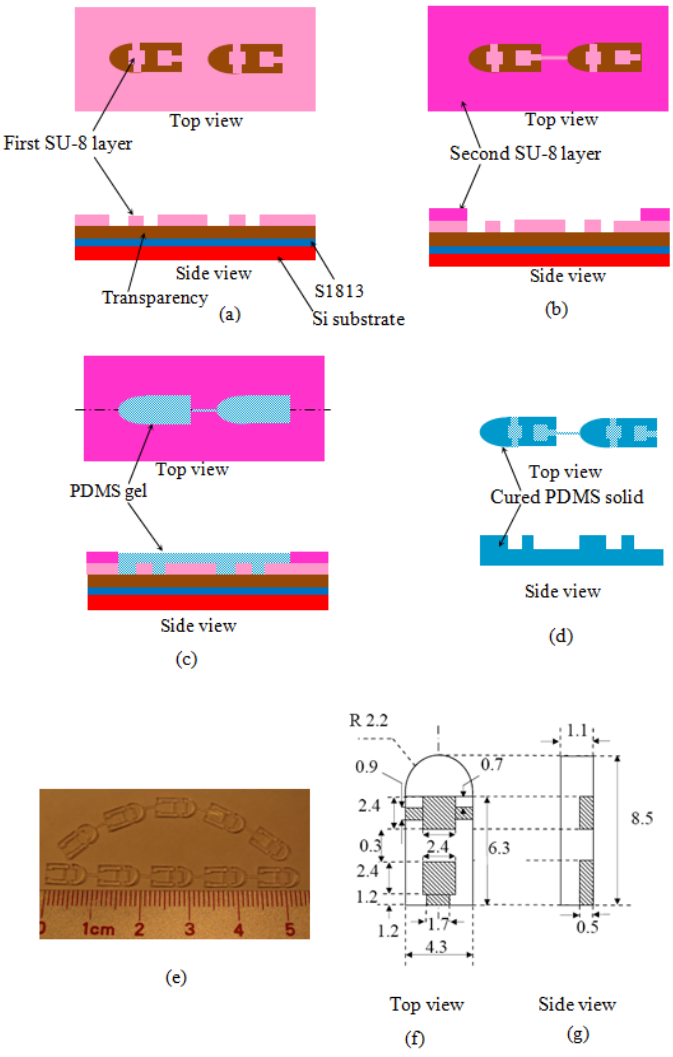

Figure 3.5 Illustration of fabrication procedure: (a) Place a transparency on an S1813-coated 4-inch silicon wafer and pattern the first SU-8 layer on the transparency using the conventional UV lithography approach; (b) Pattern the second SU-8 layer; (c) Prepare PDMS liquid gel and fill it into the SU-8 mold and (d) Cure and separate PDMS miniaturized flotillas from the SU-8 mold. (e) A representative miniaturized flotilla generated; (f) and (g) its dimensions (unit: mm).

blade. Next we put the entire wafer into a vacuum chamber for 30 minutes so that any trapped bubbles inside the PDMS liquid inside the mold could escape completely; then we cure the sample in an oven at 80 ^{o}C for two hours. Excavation of PDMS miniaturized flotilla from the SU-8 mold is conducted again with a razor blade. This process requires extra effort and may need to be accomplished under a magnifying glass due to the critical dimension of the miniaturized flotilla, which is about 300 μm. It involves separation of PDMS miniaturized flotilla from the SU-8 mold, as well as removal of extra thin layer of PDMS attached to the bottom of miniaturized flotilla which could not be scraped off in earlier step.

Two masks were applied in the second fabrication step for patterning the two layers of SU-8, respectively, using the UV lithography method. The major part of the fabrication process is similar to that used for generating a SU-8 miniaturized boat [23]. A critical difference is that a nylon wire is no longer necessary as a connector, since PDMS connectors are already patterned with other part of the miniaturized flotilla.

Two representative miniaturized flotillas generated and their dimensions are given in Fig. 3.5 (e)-(f). They had the same dimensions, and each consisted of five identical miniaturized boats. The top layer was 310 μm thick. The reservoir and nozzle of a miniaturized boat had dimensions of 2.7 mm x 2.7 mm x 310 μm and 2.4 mm x 1.4 mm x 310 μm, respectively. The bottom layer was 390 μm thick. The mass of a miniaturized boat was 18.6 mg. The total volume of the reservoir and nozzle was 3.82 μl. The PDMS connection between two neighboring miniaturized boats was 2.7 mm long and 400 μm wide. The total length of the miniaturized flotilla was 55.0 mm. Accordingly, the circular channels in which such a miniaturized flotilla could travel should have perimeters larger than 55.0 mm. That is, these channels should have radii larger than 8.8 mm. In Fig. 3.5(e), one of the miniaturized flotillas was bent to indicate that these miniaturized flotillas were bendable for making radial motions. Such a miniaturized flotilla could be further bent to form a circle of radius 8.8 mm with the first and fifth boats linked together. This implies that these miniaturized flotillas were flexible enough to travel inside the

smallest channels allowed by their length. The type of miniaturized flotillas shown in Fig. 3.5(e) was used in the tests.

3.4.2 Propulsion of PDMS flotilla

The propulsion mechanism of PDMD flotilla is similar to SU-8 flotilla as mentioned previously.

3.5 Gurgling-like Effect

3.5.1 Introduction

In a recent work, we have developed mm-scaled SU-8 boats [23]. SU-8 is a negative photoresist. The SU-8 boats were fabricated in a massive manner using ultra-violet microlithography. In order to properly apply these miniaturized structures, it is important to know how a solvent exit their reservoir, since this induces spontaneous motions of these small objects. In the case of gels, the reservoirs were all close, i.e., the reservoirs did not have top openings [35-38]. However, SU-8 boats had open reservoirs, i.e., their reservoirs had top openings [23, 58]. Thus, in this work, we considered how solvents exited both open and close reservoirs. We fabricated two cm-scaled boats of relatively large open and close reservoirs, respectively, such that we could directly observe the exit processes of solvents in these reservoirs. As in our previous work, IPA was chosen as the propellant [23, 58]. To distinguish it from water, it was dyed with a dark solution of a polymer PEDOT. Polydimethylsiloxane (PDMS), instead of opaque SU-8, was chosen as the boat material. The PDMS was transparent, allowing us to observe the movements of the IPA in the corresponding reservoirs. The density of PDMS is 0.97×10^3 kg/m^3, less than that of water (10^3 kg/m^3), enabling the PDMS boat to float on the water surface [16]. PDMS is not a photoresist material and is normally patterned by a molding process [64-69].

3.5.2 Fabrication and type of conducted tests

Figs. 3.6 (a)-(c) shows two cm-scaled PDMS boats of close and open reservoirs, respectively. For simplicity, they were called close-reservoir boat (CRB) and open-reservoir boat (ORB), separately. For comparison in their motions and in the exiting processes of IPA, the two boats had the same dimensions and differed only in the top openings of their reservoirs. The reservoir of the CRB was sealed from the top by a thin PDMS film of thickness 260 μm, while the reservoir of the ORB had a top opening.

The ORB was fabricated using a molding method with the assistance of two molds. The first mold was a plastic shell of a boat shape. It was made out of a disposable transfer pipette (VWR International Company). The tail portion of the pipette was cut off, and the head part served as the mold. This mold was used to form the body of the PDMS boat, which had the dimensions of 27 × 12.7 × 6 mm^3 (length × width × height). The second mold was a rectangular

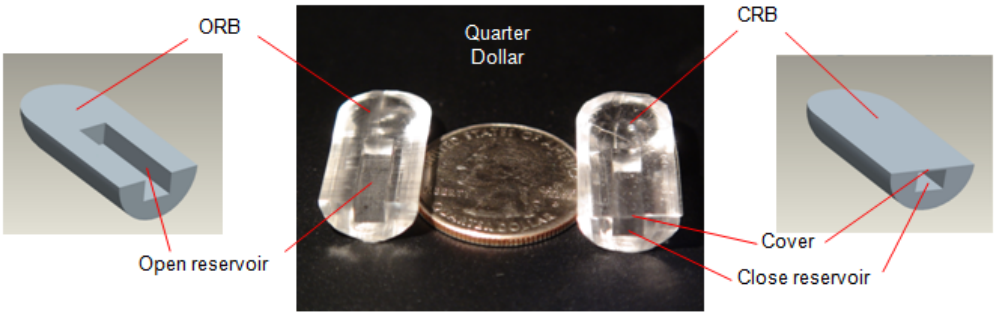

(a)

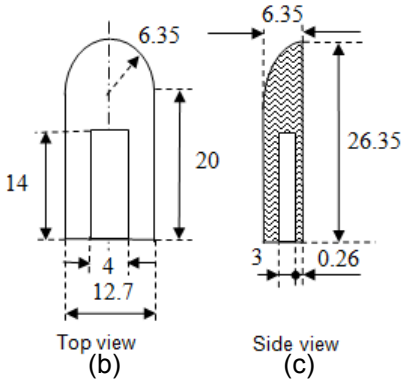

(b) (c)

Figure 3.6 Open- and close-reservoir PDMS boats, and (b) and (c) their dimensions (unit: mm).

Teflon block. It was applied to generate the reservoir, which had the dimensions of 14 × 4 × 3 mm^3 (length × width × height). Liquid PDMS (ratio between PDMS and its curing agent is 10:1) was poured inside the first mold, which was fixed by an aluminum holder, and the second mold was then inserted into the PDMS from the top (Fig. 3.7(a)). After the setup was baked at 65 °C for 10 h, the completely dried PDMS cylinder was separated from the two molds. Subsequently, the PDMS cylinder was cut off into half using a sharp knife, producing two ORBs (Fig. 3.7(b)). An additional step was included in the fabrication of a CRB. That is, a PDMS film was bonded on the top surface of an ORB to cover the top opening of its reservoir, producing a CRB (Fig. 3.7(c)).

The motions of the boats were recorded using a camcorder (model: SONY HDR500 with 30 frames per second). The camcorder was moving together with a boat in each test to capture the exit process of IPA in the reservoir, as well as to record the positions of the boat at different time instants. The videos were then played in software Adobe Premier Element to obtain the information needed.

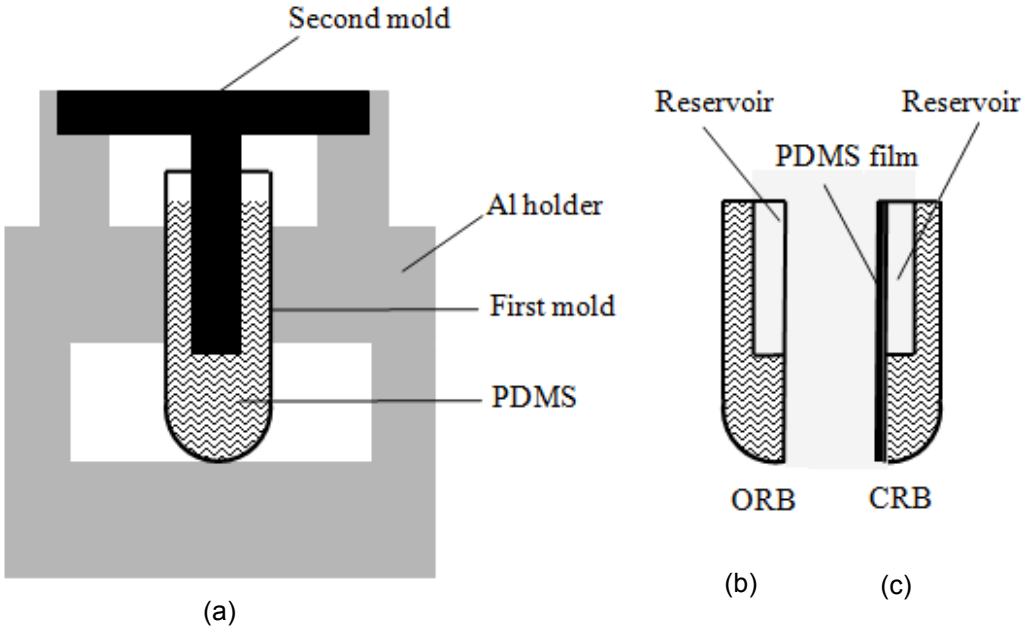

Figure 3.7 (a) Molding setup for generating ORBs. (b) Side views of an ORB (b) and a CRB (c).

The two types of boats were tested in a 2 m long, 18 mm wide and 30 mm deep, ring-shaped channel. The water was 25 mm deep. The reservoirs of the ORB and CRB had the same volume of 168 μl. The IPA was filled into the reservoir using a pipette (Nichipet EX) with the bow dipping down and the stern facing up. If the reservoir of either boat was only partially filled, then the IPA flowed slowly from the inner potion of the reservoir towards the nozzle when the boat was held horizontally with the bow slightly facing up and the stern dipping down. Three types of tests were conducted for the ORB. They differed in the amounts of the IPA loaded into the reservoir. The corresponding volumes of the loaded IPA in the three types of tests were, respectively, 30%, 60% and 90% of the volume of the boat reservoir. For simplicity, these tests were called 30%, 60% and 90% tests, separately. When the reservoir was fully filled, the IPA might spill out the reservoir during a motion. If the volume of loaded IPA was 25% or less of that of the boat reservoir, the IPA might not fully cover the bottom of the reservoir. No bubbles were trapped in the reservoir of the ORB during the three types of tests. The air that pre-existed could escape from the top opening of the reservoir when water flowed into the reservoir.

On the other hand, bubbles may appear in the tests of the CRB. The air that pre-existed was trapped in the reservoir when water behind the stern flowed into the reservoir and blocked the nozzle. When 30% to 75% of the reservoir in a CRB was filled by the IPA, an air bubble might form inside the reservoir when the CRB was placed in the water. This bubble could be removed if the CRB was held in water with the blow slightly below and stern above the water surface. Consequently, there existed a gap between the reservoir ceiling and the water surface for the potential escape of the bubble. However, it would be difficult to remove a bubble if less than 30% of the reservoir was filled with the IPA. When more than 75% of the reservoir was loaded with the IPA, not much air pre-existed in the reservoir. This pre-existing air had a chance to escape from the nozzle before the surrounding water flowed into the reservoir and blocked the nozzle. Thus, no bubbles were found in this case. To explore the motions of the CRB under different loading situations, four types of tests were conducted for the CRB: 30%

test with bubbles, 60% test with bubbles, 60% test without any bubbles, and 90% test without any bubbles. For simplicity, these tests were called 30% bubble test, 60% bubble test, 60% test and 90% test, respectively.

CHAPTER 4

RESULTS AND DISCUSSIONS

4.1 Miniaturized SU-8 Boat

Two types of tests were conducted, 1) test of the miniaturized boat's mobility in short and long channels; 2) stoppage test of the miniaturized boat.

4.1.1 Test in Short Straight Channels

This type of miniaturized boat was tested in an open channel with a length of 30 cm, which is about three times the diameter of a commonly used 4-inch silicon wafer. This channel was formed by gluing two z-shaped rulers (Office Depot) together (Fig. 4.1(a)). It had a trapezoidal cross section. The width of the top opening was 4.6 mm, the bottom 7.5 mm, and the channel height was 9.4 mm. Such a cross section would enable it to examine the sidewall effects during the motion. The markers on the rulers were used to determine the position of the miniaturized boat at a particular time. Three types of tests were conducted in the channel. They differed in the water depths, which were 1.0 mm, 5.0 mm and 9.4 mm, respectively. For simplicity, they were called 1.0 mm test, 5.0 mm test and 9.4 mm test. The volume of loaded IPA was 90% that of the miniaturized boat reservoir.

A miniaturized boat was released at one end of the channel after IPA had been filled and spread evenly in the reservoir using an Eppendorf pipette. Its motion was recorded using a camcorder (model: SONY DCR SR100 with 30 frames per second). The video was then played in software Adobe Premier Element to obtain the relationship between the position and time (Fig.4.1 (b)-(g)). This information was subsequently used to find displacement-time curves. It can be observed from Fig. 4.2 that the displacement-time relationships in these tests were

approximately linear. It took a miniaturized boat 1 s, 1.17 s and 1.83 s, respectively, to travel a distance of 30 cm when the water heights were 1.0 mm, 5.0 mm and 9.4 mm. The corresponding average speeds

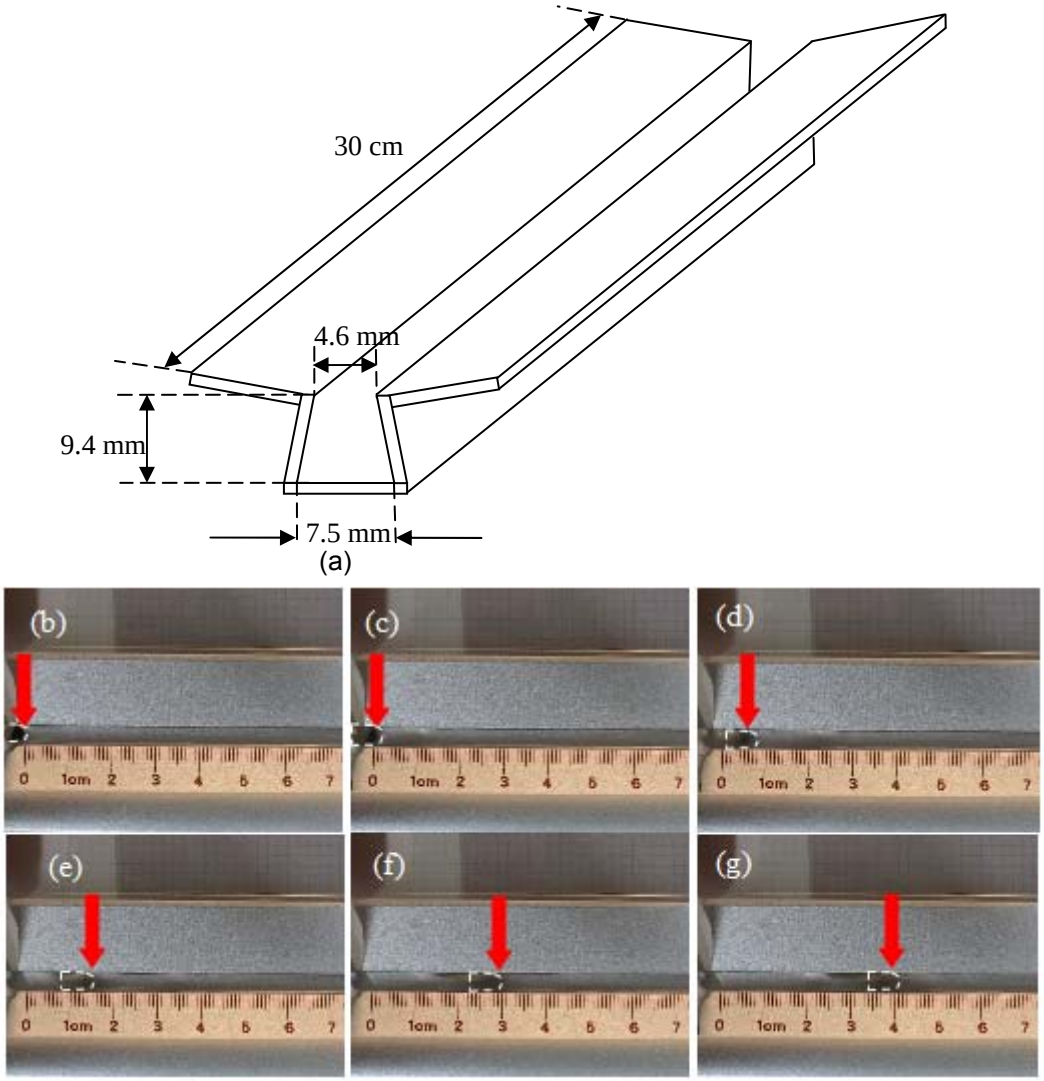

Figure 4.1 (a) Illustration of the test channel and (b)-(g) the movement sequence of the boat captured by a camcorder, and played frame by frame. The time difference between each neighboring figures is 0.1 s.

were 0.3 m/s, 0.25 m/s, and 0.15 m/s, respectively. Accordingly, Reynolds' numbers in these tests could be determined via $R_e = \frac{\rho V L}{\mu}$, where L is the length of the miniaturized boat, ρ density of water, V the speed of the miniaturized boat, and μ the dynamic viscosity of water. Reynolds' numbers were 2550,

2125 and 1275, respectively, in the three tests. Therefore, the flow type around the miniaturized boat was laminar.

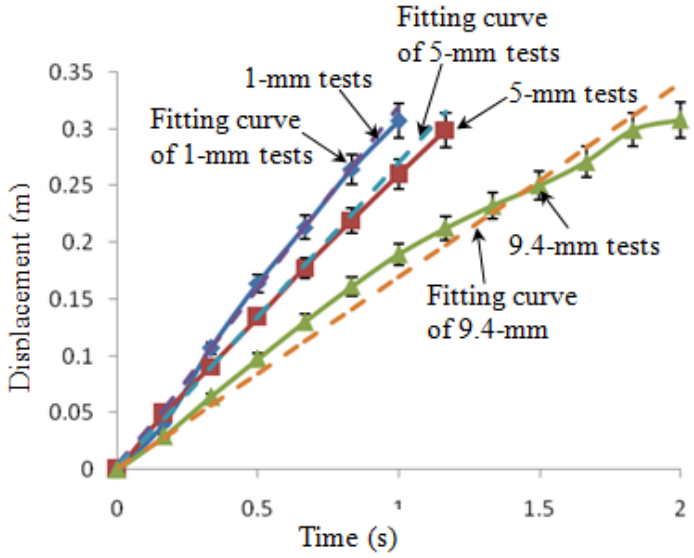

Figure 4.2 Experimental displacement-time curves in the three types of tests and the corresponding fitting curves.

To have a good understanding about the difference in displacement-time curves, a simple model was proposed to extract resistance coefficient and propulsive force. The equation of motion along the channel direction is

$$ma = \frac{1}{2}\rho C_{\rho} A V^2 + F, \quad (1)$$

where m denotes the total mass of the boat and IPA at time t, a acceleration of the boat, C_{ρ} resistance coefficient, A wetted surface area of the boat, and F propulsive force induced by the difference between the fore-and-aft surface tensions. In the above equation, $\frac{1}{2}\rho C_{\rho} A V^2$ denotes total resistance [43], including viscous resistance and wave-induced resistance. During the motion, m would decrease due to the diffusion of the IPA out of the boat. The maximum mass of IPA was 0.78 mg when the reservoir was fully filled. The mass of the boat was 19.5 mg, which is 25 times that of IPA. Therefore, the loss of IPA during the motion has negligible effect on the total mass. Accordingly, m was considered as a constant of 19.5 mg. From equation (1), the displacement-time relationship can be derived as

$$x = C_1[\frac{2ln(1+e^{c_2 t})}{C_2} - t] - \frac{2C_1}{C_2} ln2\,, \qquad (2)$$

where x and t represent displacement and time, respectively, $C_1 = \sqrt{\frac{2F}{\rho C_\rho A}}$ and $C_2 = \frac{\sqrt{2\rho C_\rho AF}}{m}$, are two constants that can be obtained through curve fitting of the displacement-time relationship; once they are known, (C_ρ, F) can be calculated from their relationship to C_1 and C_2.e.g. via curve-fitting in Fig.4.2, the sets of (C_1, C_2) for 1.0 mm, 5.0 mm and 9.4 mm tests were (0.32, 80.2), (0.27, 83.1) and (0.17, 95.9), respectively. The corresponding sets of (C_ρ, F) are calculated to be (0.144, 250 μN), (0.170, 227 μN), and (0.324, 159 μN).

Three observations can be made from these three sets of data. First, the resistance coefficient increase as the water depth increases ($C_{\rho\_1.0mm} < C_{\rho\_5.0mm} < C_{\rho\_9.4mm}$). Let d_1, d_2, and d_3 denote the gap between the miniaturized boat and the two sidewalls and the bottom surface of the channel, respectively. The corresponding sets of (d_1, d_2, d_3) in the 1.0-mm, 5.0-mm and 9.4-mm tests are (1.6, 1.6, 1.0), (0.68, 0.68, 5.0) and (0.15, 0.15, 9.4), with unit in millimeters. The gap between the miniaturized boat and the sidewall decreases as the water depth increases ($g_{side\_1.0mm} > g_{side\_5.0mm} > g_{side\_9.4mm}$), while the distance between the miniaturized boat and the bottom surface increases in the same order ($g_{bottom\_1.0mm} < g_{bottom\_5.0mm} < g_{bottom\_9.4mm}$). The majority of the miniaturized boat body (>90%) is submerged under the water, so its bottom and most of the side surfaces suffer drag forces from the water. The total area of the two side surfaces (3.27 mm^2 each) is much smaller than that of the bottom surface (34.5 mm^2). However, when the gaps between the miniaturized boat and the channel sidewalls are narrower than that between the boat and the channel bottom, they may have greater effect on resistance coefficient, as seen in the test results.

Second, F varied from 159 to 250 μN. The propulsive force may be estimated using $F = (\gamma_w \cos\theta_w - \gamma_l \cos\theta_l)d$, where γ_w, γ_l, θ_w, θ_l and d, separately, represent surface tension of water, surface tension of IPA, contact angle of water on stationary SU-8, contact angle of IPA on stationary SU-

8, and width of the region that IPA covers after exiting the rear of the boat. The measured θ_w and θ_l are 75^0 and 25^0, respectively. The value of *d* should be between the nozzle width and the boat width. Since the boats were very small, it was difficult to detect the contact angles between them and water, particularly during the boats' movement. If we assume that the two contact angles do not change during the boats' motion, then the propulsive force would be estimated through the above equation to range from 146 to 292 μN. It is interesting to see that the three calculated *F*'s from the experimental result fall within this theoretical range.

Third, the average propulsive force is different in the three types of tests. The 1-mm test involved the highest average force, while the 9.4-mm test had the lowest. During the motion, the amount of IPA in the reservoir gradually decreased through exit from the nozzle; meanwhile water kept flowing into the reservoir. These reduced the concentration of remaining IPA inside the reservoir, as well as its rate of diffusion into the environment. Consequently, the surface tension behind the boat may actually increase during the motion, and cause the reduction of the propulsive force. Therefore, the average propulsive force should decrease with the increasing time as the boat progresses. Since the travel time increased along with the water depth from 1.0 mm to 9.4 mm test, their average force decreased in the same order. In addition, the propulsive force in the three types of tests was hardly related to the total amount of water in the channel during these tests because of three reasons. First, surface tension behind the miniaturized boat was primarily affected by the IPA concentration in the vicinity of the miniaturized boat's exit. Second, IPA is lighter than water, therefore able to stay on water surface after it exits the reservoir. Third, the weight ratio of the IPA in the channel in each type of tests was far below 1% of water.

4.1.2 Test in Long Straight Channels

We then conducted tests in a long channel, which is made by connecting short channels together, as shown in Fig. 3.4(a). As the volume of loaded IPA increased from 30% to 90% with an increment of 15%, the total displacement increased from 37.0 cm to 91.4 cm. The displacements were approximately linearly proportional to the amount of loaded IPA (Fig. 4.3(b)). However, the travel time was not linearly

proportional to the amount of loaded IPA. The IPA could last 3.43 s, 4.31 s, 4.59 s, 4.64 s and 5.33 s, respectively, during the corresponding trips.

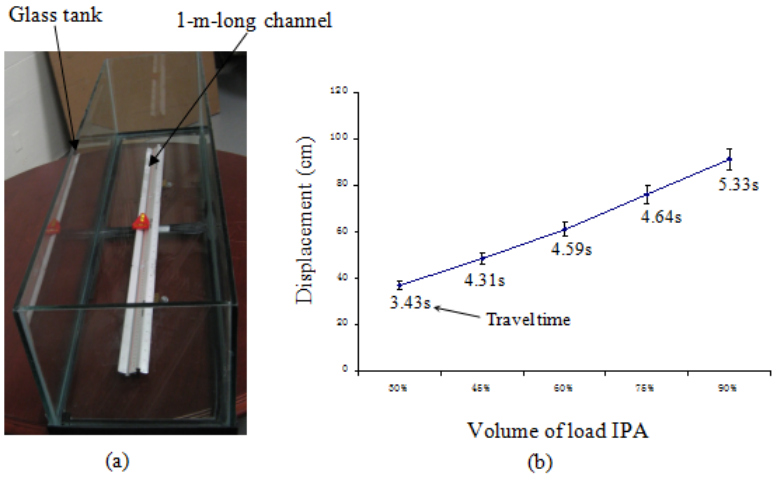

Figure 4.3 (a). Experimental setup for determining a relationship of the displacements with the amounts of loaded IPA, and (b). the relationship experimentally measured in the 9.4-mm tests.

It was also interesting to know the relationship between the displacement and the amount of IPA loaded into the boat reservoir. It was observed from Fig. 4.3 that, when the volume of the loaded IPA was 90% of that of the boat reservoir, the travel distances of the miniaturized boat were more than 30 cm in all the three types of test. In order to find the total travel distance, the length of the channel shown in Fig. 4.3 (a) was extended from 30 cm to 100 cm (including 90 cm marked length and 10 cm unmarked length) by connecting this channel with another two identical channels (Fig. 4.3 (a)). The long channel formed in such a way had a distortion of 0.5 mm, i.e., one end was about 0.5 mm higher than the other. This distortion might cause relatively large error in 1-mm tests and 5-mm tests since 0.5mm was 50% and 10% of the water depths in these two types of test, respectively. These ratios are large enough to affect the total travel distance. Therefore, we only determined the relationship of displacement with amount of IPA in 9.4-mm tests because the ratio between the distortion and water depth was relatively low (5.3%). Also, when only a small amount of IPA was loaded, it might not be able to properly cover the whole bottom of the boat reservoir; this could cause potential error. Therefore, the minimum volume of loaded IPA was chosen to be 30% of that of the boat reservoir.

Since 9.4-mm tests had the largest resistance coefficient among the three types of test, it was expected that, for a particular amount of load IPA, miniaturized boat should have longer travel distance in the other two types of tests than in 9.4-mm tests.

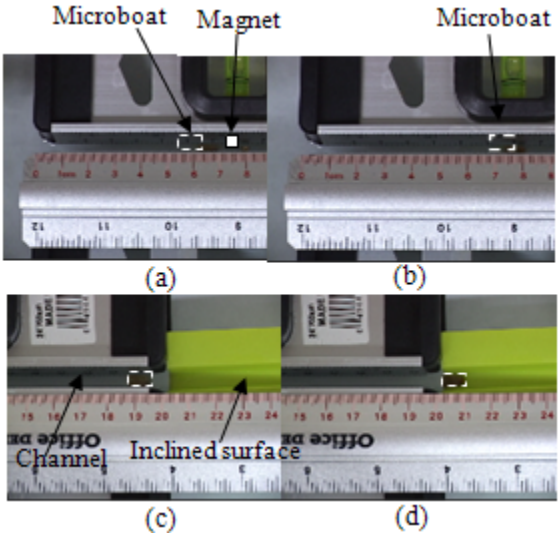

Figure 4.4 Stoppage test through magnetism and incline. (a) A miniaturized boat approached a magnet placed in the channel, and (b) it stopped on the magnet due to magnetic attraction. (c) A miniaturized boat exited from a channel and (d) it stopped on an inclined surface.

4.1.3 Stoppage Test

The third test was the stoppage of miniaturized boat. We conducted two types of experiments (1) magnetic stoppage test (Fig. 4.4(a) and Fig. 4.4(b)): a magnetic boat made by attachment of magnetic powder at the boat bottom was propelled above a permanent magnet. The magnetic force between them would stop the boat. (2) Incline stoppage (Fig. 4.4 (c) and Fig. 4.4(d)). The boat climbed onto an incline located at the end of the channel and stopped thereafter.

In the magnetic stoppage test, the bottom SU-8 layer of a miniaturized boat was coated with a layer of hard barium ferrite (NdFeB) particles, which were hard magnetic microparticles. Also, a magnet made by NdFeB was placed at the bottom of the channel for stopping the miniaturized boat via magnetic interaction. In this method, magnetostatic force was used to stop the miniaturized boat since no other external device was required and this force was easy to apply. NdFeB microparticles (UltraFine Powder Technology) has been demonstrated to be a suitable material with a relatively high remnant magnetic

moment of 8.1×10^{-5} A m^2, which implies high magnetostatic forces compared with other magnetic materials, such as Ba ferrite microparticles [39]. Therefore, it was chosen as a material for both the magnet and the magnetic coating of the boat.

Figure 4.4 (a) showed one case that a miniaturized boat was stopped on a cubic magnet with dimensions 3x3x3 mm^3 in the 7-mm test, when the magnetic force was large enough to overcome surface tension and buoyancy. Furthermore, an inclined surface could be placed at the exit of a channel to collect a miniaturized boat after its usage. The miniaturized boat started moving up along the inclined surface after it exited from the channel. Due to gravity and friction, the miniaturized boat eventually stopped on the inclined surface (Fig. 4.4(b)).

When the magnetic particle is assumed to be spherical, energy U arising from magnetic force is:

$$\begin{aligned} U &= -\frac{1}{2}mH = -\frac{1}{2}\left[V\mu_0\left(x_p - x_f\right)H\right]H \\ &= -\frac{1}{2}\left[\frac{4}{3}\pi r^3\mu_0\left(x_p - x_f\right)H\right]H \\ &= -\frac{2}{3}\pi r^3\mu_0 H^2\left(x_p - x_f\right) \end{aligned} \tag{3}$$

where x_p *and* x_f are magnetic susceptibilities of the particle and fluid.

Therefore, the magnetic force F_m that acts on the magnetic particle is given as follows:

$$F_m = -\Delta U = \frac{4}{3}\pi r^3\mu_0\left(x_p - x_f\right)H\nabla H \tag{4}$$

In our case, the bottom of the miniaturized boat is covered with magnetic particles, which we assume to be all spherical. The total magnetic force is obtained by integrating the force over the entire area:

$$F_{m-total} = \int_{bottom\ area} \frac{4}{3}\pi r^3\mu_0\left(x_p - x_f\right)H\nabla H \tag{5}$$

F_m represents the total force that was exerted on one magnetic particle, and F_s-the force obtained on a particular element in the simulation with Ansys. If these two forces are presumed to be equal, we have:

$$F_s = F_m = \frac{4}{3}\pi r^3 \mu_0 \left(x_p - x_f\right) H \nabla H \tag{6}$$

In 2-D simulation, H can be expressed as

$$H = i \cdot H_x + j \cdot H_y$$

$$\nabla H = \frac{\partial H_x}{\partial x} + \frac{\partial H_y}{\partial y}$$

$$\Rightarrow H \nabla H = \left(i \cdot H_x + j \cdot H_y\right)\left(\frac{\partial H_x}{\partial x} + \frac{\partial H_y}{\partial y}\right)$$

$$= i \cdot \left(\frac{\partial H_x}{\partial x} + \frac{\partial H_y}{\partial y}\right) H_x + j \cdot \left(\frac{\partial H_x}{\partial x} + \frac{\partial H_y}{\partial y}\right) H_y$$

Substitute into Eq. (6):

$$F_s = F_m = \frac{4}{3}\pi r^3 \mu_0 \left(x_p - x_f\right)\left[i \cdot \left(\frac{\partial H_x}{\partial x} + \frac{\partial H_y}{\partial y}\right) H_x + j \cdot \left(\frac{\partial H_x}{\partial x} + \frac{\partial H_y}{\partial y}\right) H_y\right] \tag{7}$$

Or

$$F_s = F_m = \frac{4}{3}\pi r^3 \mu_0 \left(x_p - x_f\right) \nabla H \left[i \cdot H_x + j \cdot H_y\right] \tag{8}$$

Assume the magnetic boat moves from right to left, and the magnetic force between the boat and permanent magnet originates from the boat pointing to the magnet, and the total force on the boat can be shown as in Fig. 4.5.

Before boat passes above the permanent magnet:

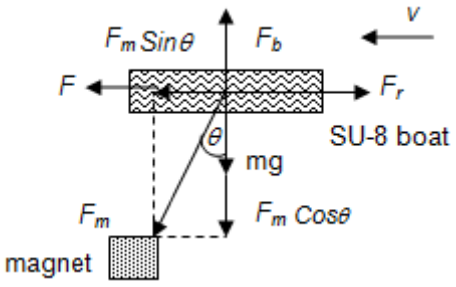

Figure 4.5 Force analysis before the boat passes the permanent magnet

In the vertical direction,

$$F_b = \rho g V = F_m Cos\theta + mg \tag{9}$$

In the horizontal direction,

$$ma = F_m Sin\theta + F - F_r = F_m Sin\theta + F - \frac{1}{2}\rho C_\rho A V^2 \quad (10)$$

Since the magnetic force in the horizontal direction adds to the propulsion force *F*, the acceleration increases, which means the velocity remains positive, so the boat keeps moving in the original direction.

After boat passes above the permanent magnet:

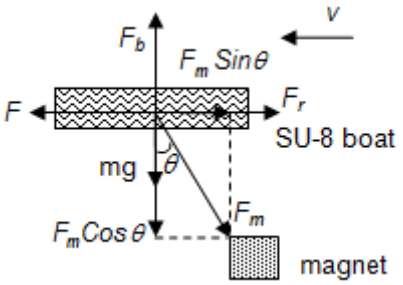

Figure 4.6 Force analysis after the boat passes the permanent magnet

In the vertical direction,

$$F_b = \rho g V = F_m Cos\theta + mg \quad (11)$$

In the horizontal direction,

$$ma = F - F_m Sin\theta - F_r = F - F_m Sin\theta - \frac{1}{2}\rho C_\rho A V^2 \quad (12)$$

Since the magnetic force in the horizontal direction is in the opposite direction to the propulsion force *F*, the acceleration decreases. If the magnetic force is large enough, the acceleration could reduce to zero even negative, thereby reducing the boat's speed till it stops, which is our objective.

4.2 Miniaturized SU-8 Flotillas

4.2.1 Test in Straight Channels

We first experimentally determined which miniaturized boat should be actuated for providing the maximum propulsive force for the miniaturized flotilla. The tests were performed in the 7-mm channel when water was 9 mm deep. Each of the five boats was chosen as the locomotive. The corresponding travel distance and average speed varied with the directly actuated boat. When the fifth boat was actuated, the miniaturized flotilla could travel through the whole channel and hit the end of the channel. This implies that the travel distance was more than 630.8 mm, which was the difference between the length of the channel and the miniaturized flotilla. The corresponding average speed was 95.2 mm/s. However, both travel distance and average speed were much less when the other four individual boats served as the locomotive. when the first, second, third and fourth boats were actuated, the travelled distance were 65.0 mm, 165.1 mm, 177.8 mm, and 277.9 mm, respectively. The corresponding average speeds were 23.6 mm/s, 13 mm/s, 23.7 mm/s and 24.2 mm/s.

These results qualitatively agreed with those obtained from the simple analysis in Section 2.3. That is, the largest propulsive force would be generated when the fifth miniaturized boat was actuated. As such, this miniaturized boat was chosen as the locomotive of the corresponding miniaturized flotilla in subsequent tests. On the other hand, it was not clear why there was much difference in the travel distances and average speeds when the first four miniaturized boats were each individually actuated. This might be caused by the different moving paths of the IPA after it exited the miniaturized boats, which could result in much difference in propulsive forces, water resistances and vertical orientations of the miniaturized boats.

The SU-8 miniaturized flotilla was tested in a straight aluminum channel, and one representative movement sequence is shown in Fig. 4.7

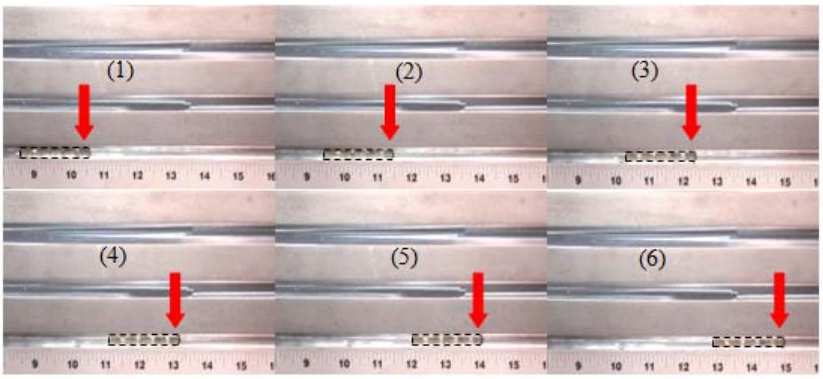

Figure 4.7 Representative movement sequences of a miniaturized flotilla in the 7-mm channel when water was 6 mm deep (the arrow indicates the location of the train head): (1) t = 3.5 s, (2) t=4.0 s, (3) t=4.5 s, (4) t=5.0 s, (5) t=5.5 s, and (6) t=6.0 s.

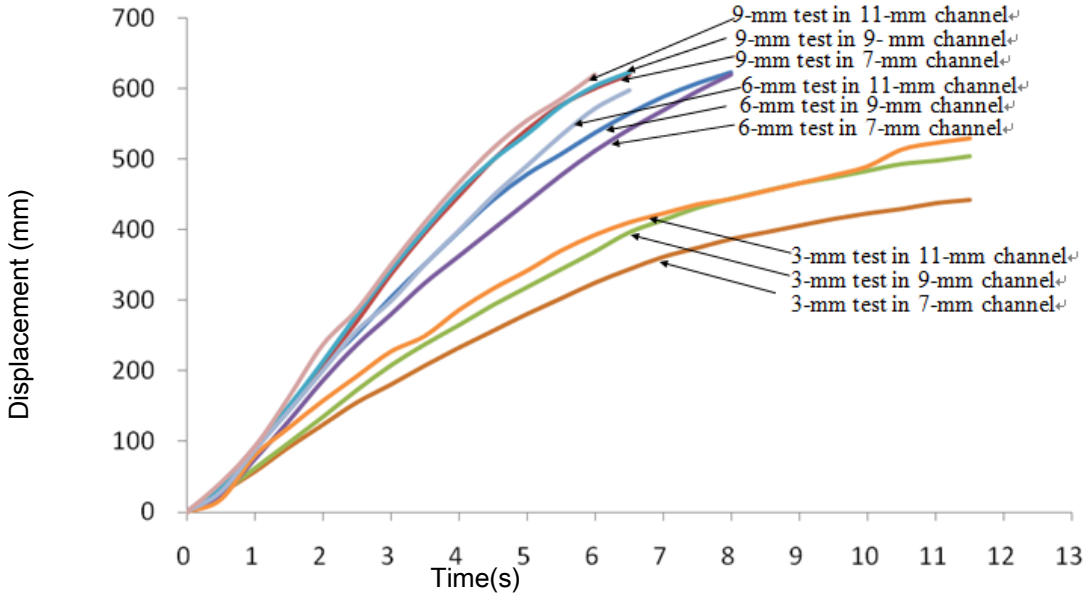

Figure 4.8 Experimental displacement–time curves in the three types of tests conducted in the three straight channels (the displacement was measured every 0.5 s with the measurement error of 0.8 mm, and the data points were not shown to see these curves clearly).

Experimental displacement-time curves in the three types of tests conducted in the three straight channels are shown in Fig. 4.8. We can observe that:

The miniaturized flotilla moved in a straight channel like a rigid object. Collisions were not observed between neighboring miniaturized boats (Fig. 4.7). The portion of the Nylon wire between two neighboring miniaturized boats, as well as the whole miniaturized flotilla, remained straight. The

propulsive force was applied on the fifth boat, and every wire connector suffered a compressive force. The propulsive force may be estimated using $(\gamma_w \cos\theta_w - \gamma_l \cos\theta_l)d$, where γ_w , γ_l , θ_w , θ_l and *d*, represent surface tension of water, surface tension of IPA, contact angle of water on stationary SU-8, contact angle of IPA on stationary SU-8, and width of the region that IPA covers after exiting the rear of the boat, respectively. The measured θ_w and θ_l are 75^0 and 25^0, separately. The value of *d* should be between the width of the nozzle and the boat.

Since the boats were very small, it was difficult to detect the contact angles between them and water, particularly when the boats were moving. If we assume that the two contact angles did not change during the motions, then the propulsive force ranged from 146 to 292 μN. Therefore, the maximum compressive force in a Nylon Wire was 292 μN. Since a wire connector would not buckle until the compressive force reached the critical load of 290 mN [16], the wire connector remained straight.

The influence of channel width and water depth on the motion of a miniaturized flotilla was specifically explored. Three types of tests were conducted in each straight channel. They differed in the water depth, which were 3.0 mm, 6.0 mm and 9.0 mm, respectively. For simplicity, they were called the 3-mm test, 6-mm test and 9-mm test. Fig. 4.8 gives the displacement-time curves obtained in these tests. The motion of the miniaturized flotilla was considered for the period when it started to move from one end of a channel till it stopped in the channel or hit the other end of the channel.

Both water depth and channel width had strong influence on the miniaturized flotilla's motion. The average speed of the miniaturized flotilla increased with the increasing water depth in each channel. For example, in the 7-mm channel, the average speeds were 40.2 mm/s, 77.4 mm/s and 95.2 mm/s, respectively, in the 3-, 6-, and 9-mm tests. Furthermore, the travel distance was also affected by the water depth. In the 3-mm tests performed in the 7-, 9-, and 11-mm channels, the miniaturized flotilla stopped in the middle of each channel, and did not go through the entire length of the channel. Its travel distances were 442.7 mm, 504.7 mm, and 528.6 mm respectively. However, in the 6- and 9-mm tests, the miniaturized flotilla hit the end of each channel, indicating its travel distance was larger than 630.8 mm, the maximum allowable travel distance in the channel.

In addition, the average speed of the miniaturized flotilla in each type of tests increased with the increasing channel width when the water levels were the same. For example, in the 3-mm tests, the average speeds were 40.2 mm/s, 45.9 mm/s, and 48.1 mm/s in the 7-, 9-, and 11-mm channels, respectively. These results indicated that the water resistance increased with the decreasing water depth and channel width. On the other hand, compared with channel width, water depth appeared to have a larger effect on the motion of a miniaturized flotilla. The average speed increased from 3-mm tests to 9-mm tests, independent of the channel width. The average speed of the 9-mm tests in the 7-mm channel (highest water level in the narrowest channel) was 95.2 mm/s. It was much higher than the average speed of the 3-mm tests in the 11-mm channel (lowest water level in the widest channel), which was 48.1 mm/s. The same applies to the travel distances. However, when the channel was very narrow, the channel width might have a larger effect than the water depth on the water resistance. For example, in [23], we found that the water resistance for a miniaturized boat was higher in a 4.6-mm-wide channel of 9.4-mm-deep water than that in a 7.5-mm-wide channel of 1-mm-deep water.

The increase of resistance due to the decrease of water depth was so-called shallow-water effect [53]. The total resistance includes viscous resistance and wave-making resistance [52]. Both increase with the decreasing water depth. According to the conservation law of mass, if the miniaturized flotilla is considered as being at rest in a flowing stream, the water passing below it in shallow water must speed up more than in deep water. Accordingly, the viscous resistance increases due to the increase of the velocity gradient (the viscous resistance is linearly proportional to this gradient); also, the wave pattern around the miniaturized flotilla changes during transition of the test from deep to shallow water [44]. The amplitude of the wave increases with the decreasing water depth. As such, wave-making resistance also increases with the decreasing water depth. Likewise, the reduction of a channel width further increases both viscous and wave-making resistances [54].

The average speed in the performed tests varied from 40.2 mm/s to 103.2 mm/s. They are lower than the average speed of a single miniaturized boat tested in a trapezoidal channel, which varied from 150 mm/s to 300 mm/s. The cross-sectional dimensions of the trapezoidal channel were comparable to

those of the straight channels used in the miniaturized flotilla tests. Naturally, this difference in the average speed was due to the fact that the miniaturized flotilla suffered a larger water resistance than each individual miniaturized boat. The water resistance was linearly proportional to both the resistance coefficient and the wetted area of a floating object. The miniaturized boats and flotillas might have different resistance coefficient since both their shapes and channel in which the tests were conducted are different. However, it is expected that the difference in wetted area between the miniaturized boats and flotillas would also cause a large difference in their water resistance. Both miniaturized boats and flotillas were submerged in the water, as observed from the relationship between their body and water. The miniaturized flotilla consisted of five miniaturized boats. Moreover, the wire connectors were wetted; so the wetted area of the miniaturized flotilla was at least five times as large as that of the miniaturized boats, causing much difference between their resistances.

4.2.2 Tests in Circular Channels

Similar to the motions in the straight channels, the miniaturized flotilla moved in the circular channel like a rigid object (Fig. 4.9). Collision was not observed between neighboring boats. A centripetal force is needed for generating radial motion of an object. In the case of an aircraft (or a bird), this force is generated by raising one wing above the other using the ailerons, which is so-called banking turn [51]. During this turn, (as shown in Fig. 4.10(a)) the aircraft experiences two forces in the vertical plane: lift and weight. The vertical component of the lift force balances the weight, while the horizontal component serves as the centripetal force. The radial motion of a car is assisted by the banked tracks (Fig. 4.10(b)). Due to this inclination of the track surface, the summation of the horizontal components of the support force and friction function as the centripetal force. The same applies to the case of macrotrains.

As for a macroboat, the centripetal force is not provided by tilt of the macroboat or the liquid surface. Instead, a rudder is used to hold the hull at an angle towards the moving direction (i.e., angle of attack) [52]. This makes the liquid resistance applying on the side of the macroboat function as a centripetal force. Unlike airplanes, cars, macrotrains and macroboats, the miniaturized flotilla we developed did not have any complicated control system, such as ailerons or rudders. Also, the water

surface was not much inclined when the micro flotilla moved inside in the circular channel. However, the miniaturized flotilla could still have channel-guided circular motions. When it was placed in the circular channel, both the first and fifth (last) miniaturized boat were against the outer sidewall of the channel (Fig. 4.10(c)), the support force applied by this sidewall made the whole train bend at the wire connectors. During the entire circular motion, these two miniaturized boats moved against the outer sidewall of the channel. In addition, as illustrated in Fig. 4.10(c)), the water resistance applying on the side of the miniaturized flotilla should push it away from the circular path. Therefore, the centripetal force should be mainly provided by the support forces of the outer sidewall.

Figure 4.9 Representative movement sequences of a miniaturized flotilla along the counter-clockwise direction in the circular channel when water was 6 mm deep: (1) t = 0 s, (2) t=0.5 s, (3) t=1.0 s, (4) t=1.5 s, (5) t=2.0 s, and (6) t=2.5 s.

It was also interesting to know the travel distance and the moving speed of the miniaturized flotilla in the circular channel. Three types of tests were conducted. They differed in the water depths, which were also 3.0 mm, 6.0 mm and 9.0 mm, respectively. As observed from Fig. 4.11, the corresponding travel distances were 498.9 mm, 653.6 mm and 782.3 mm, respectively. That is, the miniaturized flotilla travelled 1.9, 2.5 and 3.0 laps, separately, in 3-, 6-, and 9-mm tests. The corresponding average speeds were 38.1 mm/s, 51.5 mm/s, and 62.6 mm/s. These results indicated that

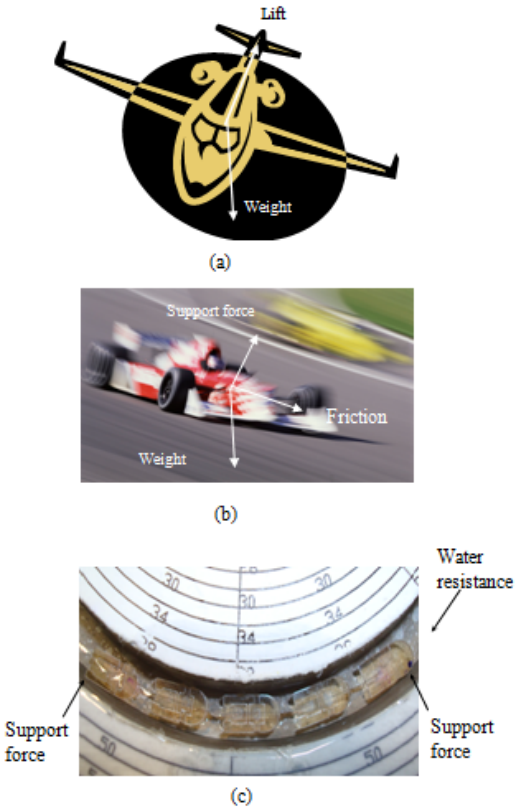

Figure 4.10 Illustration of radial turn of an airplane, a racing car, and a miniaturized flotilla
(a) Banking turn of an aircraft, (b) radial turn of a racing car, and (c) A miniaturized flotilla at rest in the circular channel (digital picture).

the water resistance also increased with the decreasing water depth in the circular motions. The circular channel had the same width as the 7-mm straight channel. The average speeds in the 3-, 6- and 9-mm tests performed in the former channel were lower than the counterparts in the same tests conducted in the latter, which were 40.2 mm/s, 77.4 mm/s and 95.2 mm/s respectively. This implies that the miniaturized flotilla suffered higher resistances in the circular channel than in the straight channel of the same width.

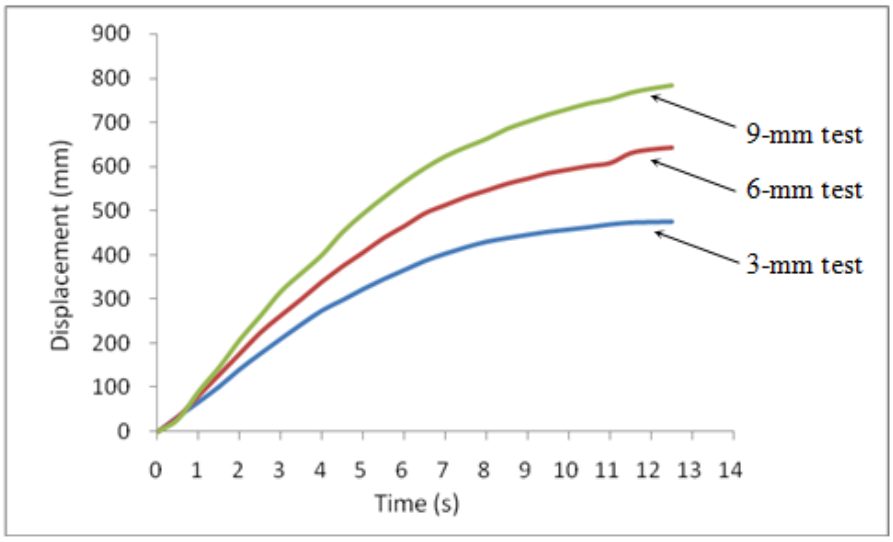

Figure 4.11 Experimental displacement-time curves in the three types of tests conducted in the 7.4-mm-wide circular channel (the displacement was measured every 0.5 s with the measurement error of 4.1 mm, and the data points were not shown to see these curves clearly).

4.3 Miniaturized PDMS Flotillas

4.3.1 Tests in Circular Channels

The PDMS flotilla was tested in a similar way as the SU-8 flotilla, which includes experiments in three straight and one circular channel. The resulting displacement-time figure is shown in Fig. 4.12.

We primarily investigated how the micro flotilla would travel under the actuation of IPA when driven by boat #5 alone. The miniaturized flotilla moved in a straight channel like a rigid object; collision was not observed between neighboring miniaturized boats, but when the water depth was less at 2mm or 3mm, the boat #5 did show signs of bending at the beginning of the actuation, especially around the tail; while this did not happen, or at least not as apparent in 6mm and 9mm tests. During these tests the PDMS connector between two neighboring miniaturized boats, even the whole miniaturized flotilla, remained straight. During all the tests, the propulsive force was applied on the fifth miniaturized boat, and every PDMS connector suffered a compressive force.

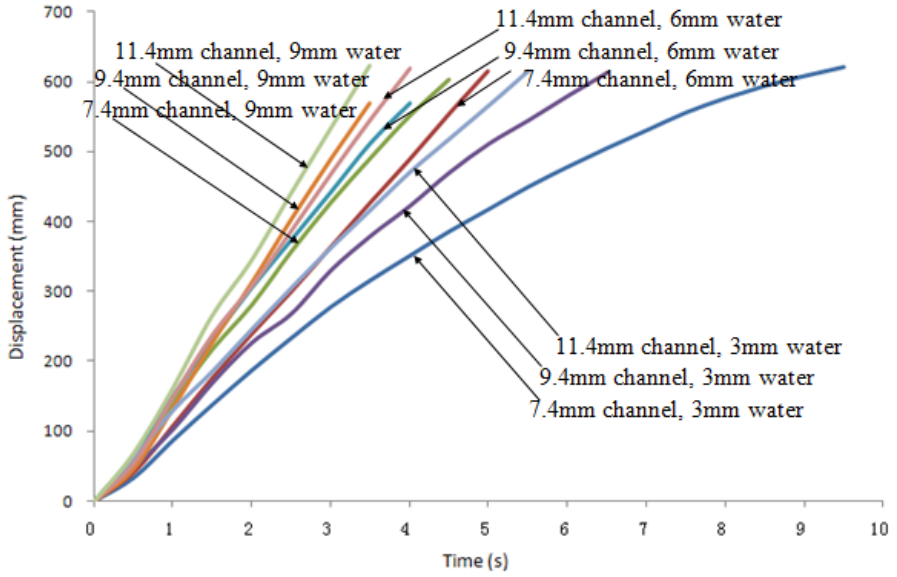

Figure 4.12 Experimental displacement-time curves in the three types of tests conducted in the three straight channels (the displacement was measured every 0.5 s with the measurement error of 0.8 mm, and the data points were not shown to see these curves clearly).

The effects of channel widths and water depths on the motion of a miniaturized flotilla were particularly explored. Four types of tests were conducted in each straight channel. They differed in the water depths, which were 2.0mm, 3.0 mm, 6.0 mm and 9.0 mm, respectively. For simplicity, they were called the 2-mm test, 3-mm test, 6-mm test and 9-mm test, separately. Figure 4.12 gives the displacement-time curves obtained in the 3mm, 6mm and 9mm tests. The motion of the miniaturized flotilla was measured for the period since it started to move at one end of a channel till it stopped somewhere in the channel or hit the other end of the channel.

Both water depths and channel widths had much influence on the flotilla's motions. The average speed of the miniaturized flotilla increased with the increasing water depth in each channel. For example, in the 7-mm channel, the average speeds were 65.3 mm/s, 123.2 mm/s and 134.1 mm/s, respectively, during the 3-, 6-, and 9-mm tests. Unlike what was observed in the previous work, the travel distances were not affected considerably by water depths. During all these tests, almost all the miniaturized flotilla made through the entire channel (even the 2-mm test), indicating their travel distance was greater than

630.8 mm, the maximum allowable travel distance in the channel. In addition, the average speed of the miniaturized flotilla in each type of tests increased with the increasing channel width while the water levels were the same. For example, in the 3-mm tests, the average speeds were 65.3 mm/s, 94.3 mm/s, and 111.7 mm/s, respectively in the 7-, 9-, and 11-mm channels. These results indicated that the water resistance increased with the decreasing water depth and increasing channel width. On the other hand, compared with channel width, water depth appeared to have a larger effect on the motion of a miniaturized flotilla.

The average speed increased from 3-mm to 9-mm tests, independent of the channel width. The average speed of the 9-mm test in the 7-mm channel (highest water level in the narrowest channel) was 134.1 mm/s, much higher than that of the 3-mm test in the 11-mm channel (lowest water level in the widest channels), which was 111.7 mm/s. The same applies to the travel distance. However, when the channel was very narrow, the channel width might have a larger influence on the water resistance than the water depth. For example, in [23], we found that the water resistance for a miniaturized flotilla was higher in a 4.6-mm-wide channel of water depth 9.4-mm than that in a 7.5-mm-wide channel of water depth 1-mm.

The increase of resistance due to the decrease of water depth is the so-called shallow-water effect [52]. The total resistance includes viscous resistance and wave-making resistance [53]. Both increase with the decreasing water depth. According to the conservation law of mass, if the miniaturized flotilla is considered as being at rest in a flowing stream, the water passing below it must speed up more in shallow water than in deep water. Accordingly, the viscous resistance increases due to the increase of the velocity gradient (the viscous resistance is linearly proportional to this gradient); also, the wave pattern around the miniaturized flotilla changes from deep to shallow water during the transition [53]. The amplitude of the wave increases with decreasing water depth. As such, wave-making resistance also increases with decreasing water depth. Likewise, the reduction of a channel width further increases both viscous and wave-making resistances [54].

The average speed in the performed tests varied from 65.3 mm/s to 177.8 mm/s. They were lower than the average speed of a single miniaturized boat tested in a trapezoidal channel, which varied from 150 mm/s to 300 mm/s. The cross-sectional dimensions of the trapezoidal channel were comparable to those of the straight channels used in this test. Naturally, this difference in the average speed was due to the fact that the miniaturized boat suffered a smaller water resistance. The water resistance was linearly proportional to both the resistance coefficient and the wetted area of a floating object. The miniaturized boats and flotillas might have different resistance coefficients since both their shapes and channels where the tests were conducted are different. However, it is expected that the different wetted areas between the miniaturized boats and flotillas should also cause a large difference in their water resistance. The miniaturized flotilla consisted of five miniaturized boats; however, both miniaturized boats and flotillas were almost completely submerged in the water, as observed from their relationship to the water surface. Moreover, the PDMS connectors were wetted. Thus, the wetted area of the miniaturized flotilla was at least five times as large as that of an individual miniaturized boat, causing much difference between their resistances.

4.3.2 Tests in Circular Channels

As for a macroboat, the centripetal force is not provided by tilt of the macroboat or the liquid surface. Instead, a rudder is used to hold the hull at an angle towards the moving direction (i.e., angle of attack) [52]. This makes the liquid resistance applying on the side of the macroboat function as a centripetal force. Unlike airplanes, cars, macrotrains and macroboats, the miniaturized flotilla we developed did not have any complicated control system, such as ailerons or rudders. Also, the water surface was not much inclined when the micro flotilla moved inside in the circular channel. However, the miniaturized flotilla could still have channel-guided circular motions. When it was placed in the circular channel, both the first and fifth (last) miniaturized boat were against the outer sidewall of the channel (Fig. 4.10(c)), the support force applied by this sidewall made the whole train bend at the wire connectors. During the entire circular motion, these two miniaturized boats moved against the outer sidewall of the channel. In addition, as illustrated in Fig. 4.10(c), the water resistance applying on the side of the

miniaturized flotilla should push it away from the circular path. Therefore, the centripetal force should be mainly provided by the support forces of the outer sidewall.

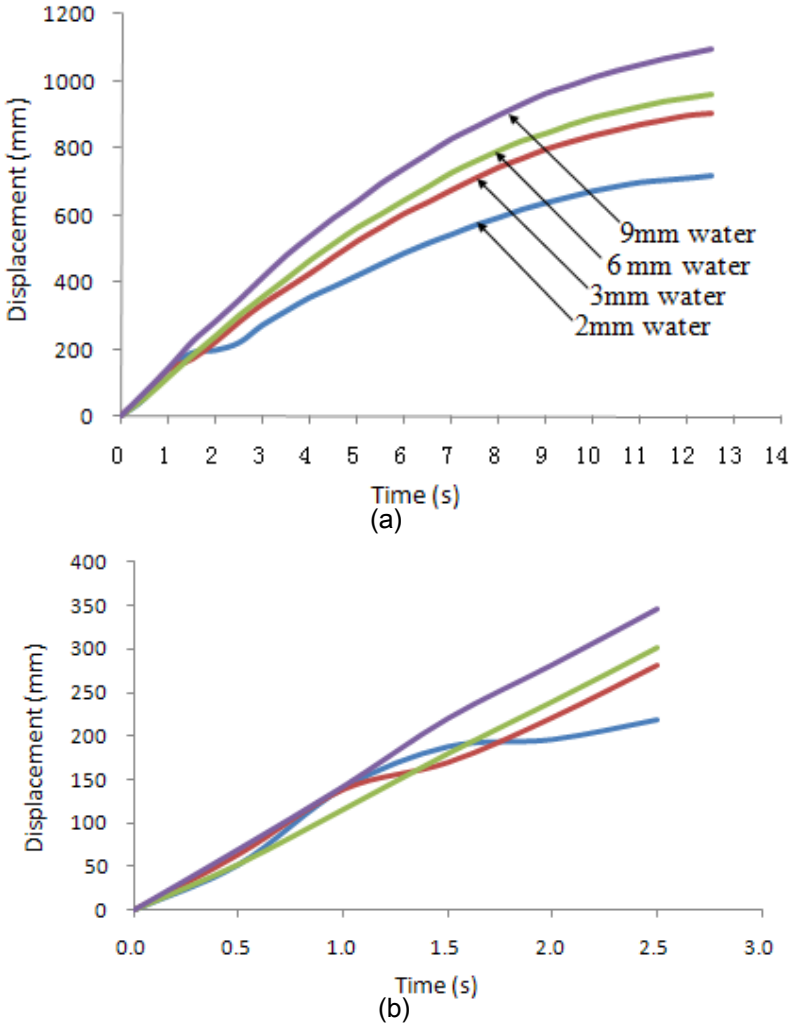

Figure 4.13 Experimental displacement-time curves in the 7 mm channel under different water depth (the displacement was measured every 0.5 s with the measurement error of 0.8 mm, and the data points were not shown to see these curves clearly). (a) The whole traveling distance (b) Only the first three seconds.

It was also interesting to know the travel distance and the moving speed of the miniaturized flotilla in the circular channel. Four types of tests were conducted. They differed in the water depths, which were also 2.0 mm, 3.0 mm, 6.0 mm and 9.0 mm, respectively. As observed from Fig. 4.13, the corresponding travel distances were 727.9 mm, 923.6 mm, 989.6 mm and 1127.7 mm, respectively. That is, the miniaturized flotilla travelled 2.8, 3.5, 3.8 and 4.3 laps, separately, in 2-, 3-, 6-, and 9-mm tests. The

corresponding average speeds were 50.2 mm/s, 63.7 mm/s, 66.0 mm/s, and 75.2 mm/s. These results indicated that the water resistance also increased with the decreasing water depth in the circular motions. The circular channel had the same width as the 7-mm straight channel. The average speeds in the 2-, 3-, 6- and 9-mm tests performed in the former channel were lower than their counterparts in the latter channel, which were 57.8 mm/s, 65.3 mm/s, 123.2 mm/s and 134.1 mm/s respectively. This implies that the miniaturized flotilla suffered higher resistances in the circular channel than in the straight channel of the same width.

4.4 Gurgling-like Effect

4.4.1 Results of the ORB

4.4.1.1 Exchange processes of water and IPA

In the 30%, 60% and 90% tests of the ORB, we found that the exiting process of the IPA from the reservoir was actually an exchange process of water and IPA. That is, when the IPA exited the reservoir, water flowed into the reservoir at the same time. According to the in-situ observation of the motion in each test (Fig. 4.14), three factors mainly affected the exchange process: difference between surface tensions of water and IPA, a free convection flow due to gravity, and binary diffusion between the IPA and water. Surface tension gradients may induce the movement of a liquid droplet on the surface of another liquid. For example, when a drop of alcohol is laid on the middle of water, water rushes away from the middle, creating a hollow spot. Since water has a higher surface tension than alcohol, more watery portion draws itself away from the more alcoholic portion, as interpreted by Thomson [72]. These surface tension-driven motions of liquids are so-called Marangoni effect [21, 68-70]. This effect was also considered to be the main factor that induced squat and trim phenomena in an mm-scaled SU-8 boat [58]. In this work, we did not observe dramatic squat and trim phenomena during the tests of the ORB probably due to the fact that the cm-scaled ORB was much larger than the mm-scaled SU-8 boat. Consequently, Marangoni effect could not make the ORB have dramatic translational and rotational movements in the vertical plane. The same applied to the CRB.

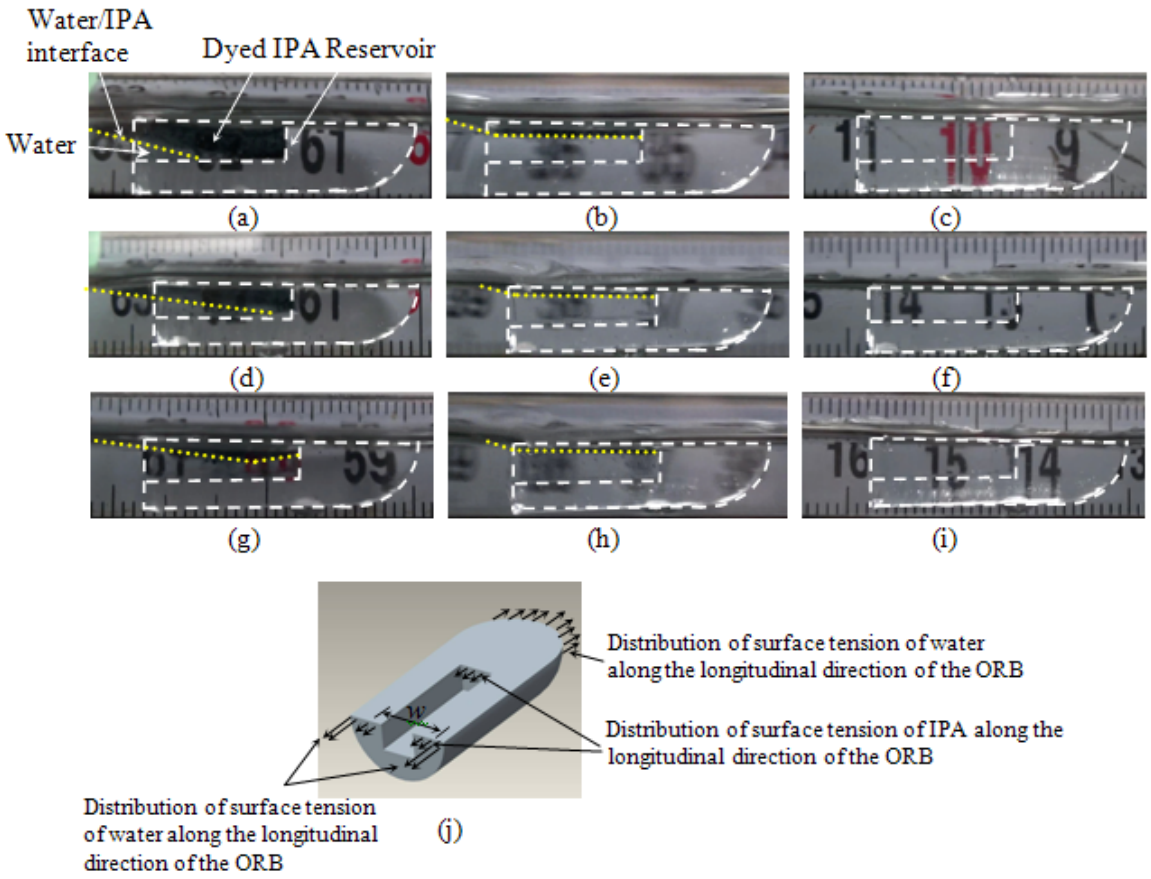

Figure 4.14 In-situ observation of the exchange processes of water and IPA in the reservoirs of the ORB (side views). 90% test: (a) in the beginning at *t*=0.07 s, (b) in the middle at *t*=4.43 s and (c) at the end of a motion at *t*=9.5 s. 60% test: (d) in the beginning at *t*=0.03 s, (e) in the middle at 4.23 s and (f) at the end of a motion at *t*=9 s. 30% test: (g) in the beginning at *t*=0.07 s, (h) in the middle at *t*=4.13 s and (i) at the end of a motion at *t*=9 s. (j) Distribution of fore-and-aft surface tensions along the longitudinal direction of the ORB.

Take the motion in the 90% test as an example. Once the ORB was placed in water and IPA had initial contact with water, the IPA was drawn out of the reservoir along the water surface due to Magrangoni effect. In the meanwhile, convection flow was also observed (Figs. 4.14(a) and 4.14(b)). Water entered the reservoir and pushed IPA upwards, because the density of IPA was smaller than water (a process of free convention [64]). Water stayed in the bottom portion of the reservoir, while IPA was on the top level. The continuous flow of water into reservoir and loss of IPA made the IPA layer become thinner (Fig. 4.14(b)). Accordingly, the interface between the water and IPA gradually moved upwards and

inwards inside the reservoir. In the meantime, the color of the dyed IPA became lighter due to the binary diffusion between the IPA and the underneath water. Distributions of fore-and-aft surface tensions along the longitudinal direction of the ORB were illustrated in Fig. 4.14(j). The difference between the fore-and-aft surface tensions provided a propulsive force to drive the ORB forward. There existed IPA beside the inner sidewall of the reservoir until water completely occupied the reservoir. The difference between the surface tension of this portion of IPA and that of water in front of the boat also contributed to the propulsive force. Once all the IPA got out of the reservoir and water occupied the whole reservoir (Fig. 4.14(c)), the driving force became zero since there was no difference between fore-and-aft surface tensions. Figures 4.14(d) - 4.14(f) show the exchange process of dyed IPA in the ORB reservoir for the 60% test and 4.14(g) - 4.14(i) give that for the 30% test. The exchange processes of IPA and water in these two types of tests were similar to that in the 90% test, although the amounts of the loaded IPA in the 30% and 60% tests were different.

4.4.1.2 Exchange process of water and IPA in the shallow reservoir

In our previous work, the reservoir of an mm-scaled SU-8 boat was empty after IPA exited the reservoir [58]. However, in this work, the reservoir of the ORB was filled with water at the end of the motion. In order to understand the reason behind, a test station was set up to observe the exchange process of IPA and water in the reservoir of a stationary ORB. The ORB was fixed in a plastic container using tweezers with the bow slightly facing up and the stern dipping down such that the loaded IPA could gradually flow to the reservoir nozzle to have initial contact with surrounding water. The plastic container had dimensions of 8.0 × 8.0 × 1.5 cm^3 (length × width × height) (Fig. 4.15(a)). Let h denote the vertical distance between water surface and the bottom of the ORB reservoir (Fig. 4.15(b)). In the previous tests described in Sub-section 4.4.1.1, the ORB was almost completely submerged inside water, i.e., h=3.0 mm. Compared with the ORB, the SU-8 boat had a shallow reservoir, which was 0.14 mm deep. To understand the exchange process of water and IPA in a shallow reservoir, in the present tests, we also considered the situation that the ORB was just partially submerged in water. That is, only part of the ORB reservoir was below the water surface. Therefore, in the present tests, h ranged from 0.1 mm to 3.0 mm

(the measurement error was ± 0.2 mm). In each of these tests, the volume of the loaded IPA was 60% of that of the ORB reservoir.

Depending on the values of h, three different phenomena were observed in the present tests: (I) if $h \leq 1.3$ mm, then the reservoir was empty at the end of the test and no water flowed into the reservoir during the test; (II) if 1.3 mm$< h \leq$ 2.3 mm, then the reservoir was empty at the end of the test while water flowed into the reservoir during the test; and (III) if 2.3 mm$< h \leq$ 3.0 mm, then the reservoir was filled by water at the end of the test. The filling results observed in the SU-8 boat and the ORB belonged to the first and third cases, respectively.

In Case I, as shown in Figs. 4.15(c) - Fig. 4.15(e) when h was 1.2 mm, the IPA in the reservoir was drawn out of the reservoir after it had initial contact with water at the nozzle of the reservoir. No water flowed into the reservoir during the exiting process of the IPA. In Case II, if h was 2.3 mm, the first half of the exchange process was similar to that in Case I, while the second half was different (Fig. 4.15(f) and 4.15(g)). In the second half of the exchange process, a hollow spot was observed at the inner end of the reservoir (4.15(g)). This hollow spot gradually increased its size, and eventually pushed all the pre-existing water out of the reservoir, resulting in an almost empty reservoir at the end of the test (4.15(h)). In Case III, when h was 3.0 mm, the exchange process in the corresponding test was similar to what was observed in the three types of the ORB tests (4.15(g)). Water filled the reservoir at the end of the test. The difference in the filling results of the three cases was induced by the interplay among Magrangoni effect, free convection, and recovery of a hollow spot by surrounding water.

Once the IPA exited the reservoir and had contact with water, due to Marangoni effect, water rushed away from the reservoir, creating a hollow spot behind the stern. In the meanwhile, water surrounding the hollow spot flowed into the spot to fill it up. The size of the generated hollow spot was related to the water depth behind the stern. According to our previous tests on mm-scaled SU-8 boats [58], when water was 2.0 mm deep or below, the largest hollow spot generated was as deep as the original water depth in a 7-mm-wide glass channel, and no water was left underneath this hollow spot. If water was more than 2.0 mm deep, then the largest hollow spot was not as deep as that in the shallow

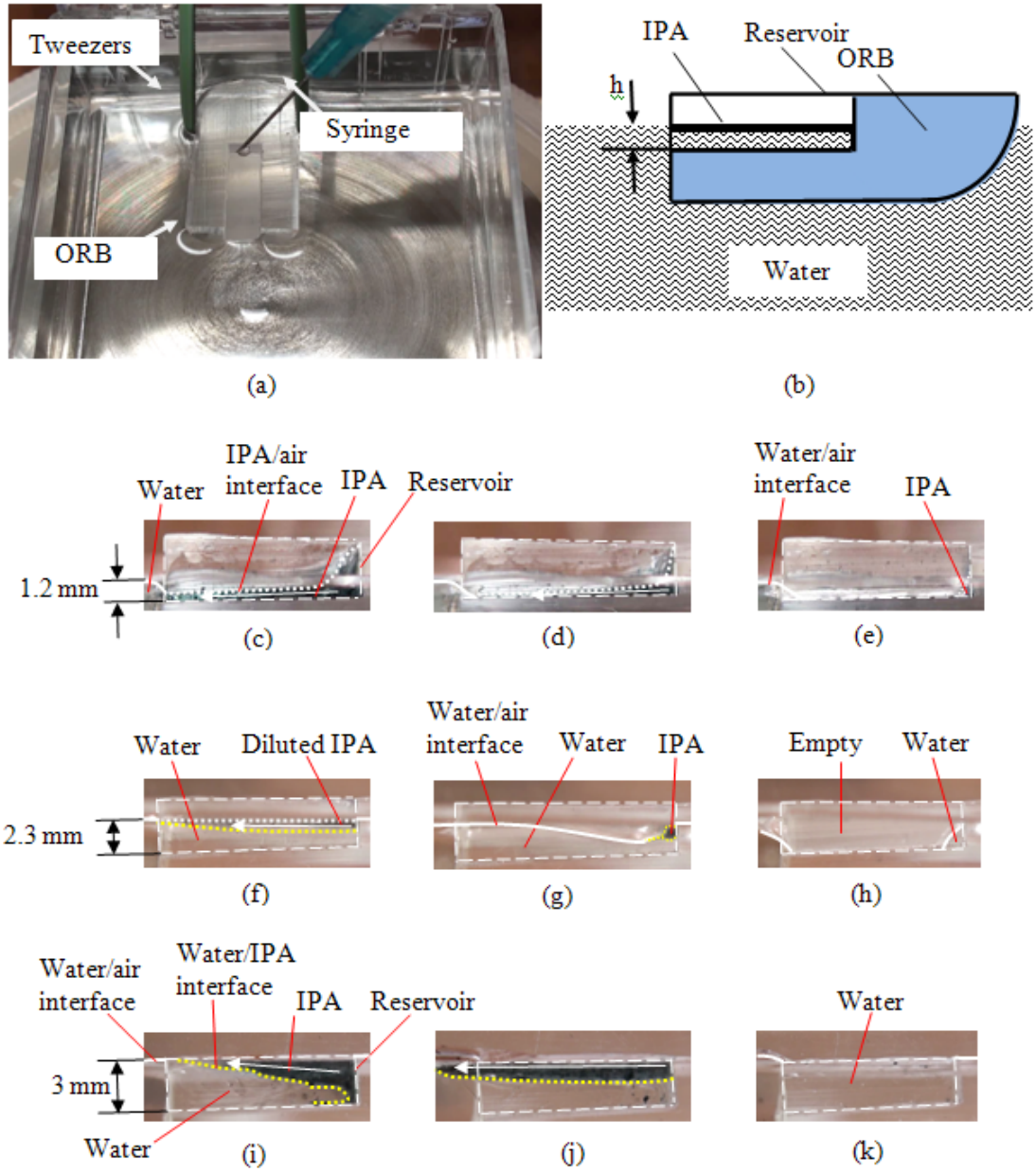

Figure 4.15 Observation of the exchange processes of water and IPA in the reservoir of the ORB in shallow water (side views). (a) Set up of the test station, and (b) its schematic. In case h=1.2 mm, the process (c) at t=6.1 s, (d) at t=23 s and (e) at t=59.3 s. In case h=2.3 mm, the process (f) at t=2.7 s, (g) at t=14 s and (h) at t=22.6 s. In case h=3 mm, the process (i) at t=0.2 s, (j) at t=1.3 s and (k) at t=8.2 s.

water. Also, this hollow spot was more quickly filled by surrounding water. As the original water depth was 2.5 mm and above, the largest hollow spots remained to be 1.0 mm deep, indicating that water would not have a chance to flow into the reservoir if *h* is not much larger than 1.0 mm. This interpreted the filling

phenomenon observed in Case I. If 1.3 mm<$h \leq$2.3 mm, which was Case II, water at the bottom of the hollow spot was able to get into the reservoir due to the difference between the densities of water and IPA, which generated a force to push water into the reservoir. The water in the reservoir was covered by an IPA layer during the major part of the exchange process, and there was not vertical interface between the IPA and the water. Accordingly, no hollow spot was generated. At the end of the exchange process, most of the IPA in the reservoir had flowed out of the nozzle. There only existed IPA behind the inner sidewall of the reservoir. This created a relatively vertical interface between this part of the IPA and water inside the reservoir (4.15(g)). Accordingly, due to Magrangoni effect, a hollow spot was created. Water surrounding the hot spot was shallow and not quick enough to fill this hollow spot. On the other hand, the continuous spreading of the IPA on the surface of the hollow spot made more water rush away from the reservoir. Eventually, all the water that pre-exited in the reservoir flowed out of the reservoir, generating an empty reservoir. However, in Case III, the water surrounding the hollow spot was deep enough to fill it. Although part of the water pre-exited in the reservoir might flow out of the reservoir because of Magrangoni effect, the continuous flow of water into the reservoir made up this loss and still filled the reservoir at the end of the test.

4.4.1.3 Experimentally obtained relationships

Figure 4.16 gives speed-time relationships of the ORB obtained in the tests. As observed from these experimental relationships, the ORB reached its highest speed in a short time, and then continued to decrease until it finally stopped. Such variation in the speed was similar to what was observed in the translational motion of a gel [37].The motion in each test could be divided into three stages according to the variation of the speed. In Stage A, the speed first had a rapid increase and then a sharp decrease. In Stage B, the speed did not have much change, while in Stage C the speed had a rapid decrease. Take the 60% test as an example (Fig. 4.16). The three stages lasted about 2.5 s, 3.0 s and 3.5 s, respectively. In Stage A, the speed of the ORB increased from 0 to the maximum value of 8.4 cm/s at t=2.0 s, and then dropped down to 8 cm/s at t=2.5 s. The average acceleration in Stage A was 3.2 cm/s^2. In Stage B, the ORB reduced its speed very slowly from 8 cm/s at t=2.5 s to 7.2 cm/s at t=5.5 s. The average

acceleration in this stage was -0.27 cm/s^2. In Stage C, the ORB quickly reduced its speed from 7.2 cm/s to 0 within 3.5 s. The average acceleration in this stage was -2.1 cm/s^2. The time period and speed in each stage may vary with the type of test. In the 30% tests, the time periods for the three stages were 2.0 s, 3.0 s, and 4.0 s, respectively, while in the 90% test, the time periods for the three stages were 2.5 s, 4.0 s, and 3.0 s, respectively. The total travel times of the ORB in 30%, 60% and 90% tests were 9.0 s, 9.0 s and 9.5 s, respectively. Generally, the speed in the 90% test was slightly higher than that in the 60% test, and relatively much higher than that in the 30%. The average speeds of the ORB in the 90%, 60% and 30% tests were 6.1 cm/s, 6.1 cm/s and 5.2 cm/s, respectively. Accordingly, the ORB had the longest and shortest travel distances in the 90% and 30% tests, separately. The total travel distances of ORB in the 90%, 60% and 30% tests were 57.9 cm, 55.1 cm and 46.8 cm, respectively.

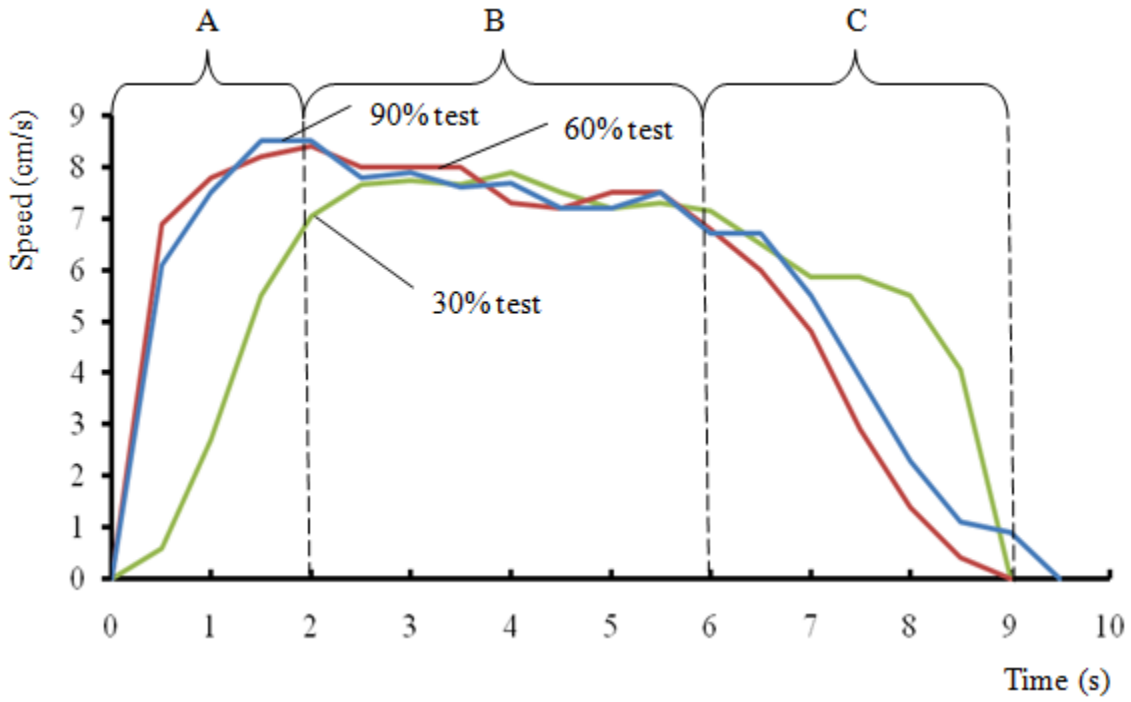

Figure 4.16 Speed-time relationships of the ORB.

Small particles have been previously applied in, for example, reference 70 to determine the spreading speed of aliphatic alcohol on a water surface. In this work, we used blue powders (extra fine glitters of Horizon Group Company) to find the coverage of the IPA on the stern in the 30%, 60% and

90% tests. Once the IPA exited the nozzle of the reservoir, it immediately spread on the water surface due to the difference between the surface tensions of the IPA and water. This spreading drove the blue powders away. Based on flowing patterns of these blue powders, we could determine the coverage of the IPA behind the stern. According to our observation, the IPA covered the entire stern during the whole motion in each of the 30%, 60% and 90% tests. Therefore, the coverage of the IPA on the stern did not vary with time and had a constant value of 12.7 mm, which equals the width of the boat's stern.

According to the video of a motion, the portion of the reservoir occupied by the dyed IPA at a time instant could be identified (Fig. 4.14). Based on this information, we determined the amounts of the IPA in the reservoir at different time instants during the 30%, 60% and 90% tests (Fig. 4.18). The amount of the IPA given in this figure was expressed in the form of the volume percentage, i.e., the percentage of the reservoir volume occupied by the IPA, and represented by v_1%. It can be observed from Fig. 4.15 that the amount of the IPA during a motion decreased with time. In the 90% test, the amount of the IPA had a sharp drop during the first 0.5 s, and decreased from 90 v_1% to 53 v_1% during this period. The reduction rate was 74 v_1%/s. After that, the amount of the IPA decreased with time in an approximately linear manner at a rate of 6.0 v_1%. In the 60% test, the sharp drop in the amount of the IPA occurred during the first 1.0 s, and the reduction rate was 22 v_1%/s. Subsequently, the amount of the IPA decreased with time in an approximately linear manner at a rate of 4.7 v_1%/s. The sharp change in the 90% and 60% tests at the beginning of a motion might be due to the large vertical interface of the IPA and water at the reservoir nozzle (Fig. 4.14 (a1) and 4.14(b1)). These made much IPA flow out of the nozzle at the beginning of the motion. After that, the contact area of the two liquids at the nozzle was reduced (Fig. 4.14 (a2) and 4.14 (b2)), and the flowing rate became relatively stable. In the 30% test, since the initial contact area between water and IPA was relatively small (Fig. 4.14(c1)), a sharp loss of the IPA was not found at the beginning of the corresponding motion. The amount of the IPA decreased with time in an approximately linear manner at a rate of 3.3 v_1%/s.

4.4.1.4 Propulsive forces and IPA concentration

Two factors may contribute to the propulsion: the exit of IPA from the reservoir, and the difference between fore-and-aft surface tensions. The first factor was the dominant one in the propulsion of a jet plane [65], a squid [66, 67] or a cuttlefish [67]. It was also considered to be the dominant factor in the case of gel propulsion [35-38]. When a liquid or gas flows out of its container at a certain speed, due to conservation of linear momentum, a force is produced, which drives the container to move along the opposite direction. The second factor is surface tension gradient around a solid object. As a solvent exits a solid object, surface tension behind this object is reduced. This creates surface tension gradient around the solid object, making it move on a water surface. As demonstrated below, the second factor was considered to be the dominant one in the case of the ORB, as well in that of mm-scaled SU-8 boats [23,58], and the first factor was negligible in both cases.

Due to conservation of linear momentum, the propulsive force, F_1, induced by the exit of the IPA is

$$F_1 = v_1 \frac{dm_1}{dt}, \tag{14}$$

where m_1 denotes the mass of the IPA loaded into the reservoir, *t* time, and v_1 the exiting speed of the IPA at the nozzle of the reservoir. Next, let's estimate an upper limit of F_1. Assume that the reservoir is fully filled by IPA. The density of dyed IPA was measured to be 0.77 g/cm^3. Accordingly, m_1 =0.13 g. The spreading speed of IPA on water surface decreases with its concentration, and the highest spreading speed, which corresponds to pure IPA, is 39 cm/s.[12] Also, assume that the IPA exits the boat at this speed. According to Fig. 4.18, the maximum volume change rate of the IPA in the reservoir during the three types of tests was 74 v_1 %/s. The corresponding value of $\frac{dm_1}{dt}$ was the largest and equaled 0.097 g/s. Then, by equation (1), an upper limit of F_1 is 38 μN. Next, let's consider the propulsive force induced by the second factor. The dynamic contact angles observed at the stern and

bow of the ORB during the motions were both 90°. Let F_2 denote the propulsive force induced by the difference between surface tensions of IPA and water. We have

$$F_2 = (\gamma_w - \gamma_l)w, \tag{15}$$

where γ_w and γ_l denote surface tensions of water and IPA, respectively, and *w* represents the width of the portion of the stern covered by IPA (Fig. 4.14(d)). The value of γ_w is 72.8 mN/m. As shown in Fig. 4.19, the value of γ_l increases with the decrease in the volume concentration of the IPA in its solution (represented by v_2% in this work), and varies between 22.6 mN/m and 30.0 mN/m when the IPA concentration decreases from 100 v_2 % to 31 v_2 %. This relationship was obtained according to experimental data given in reference 71.

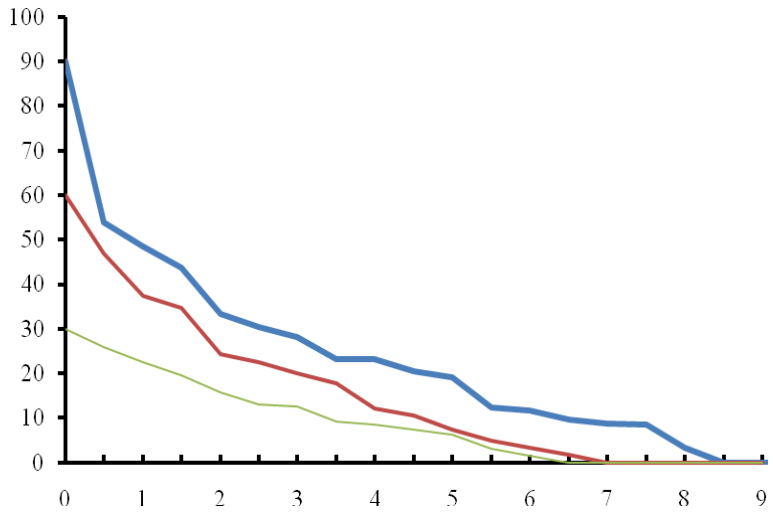

Figure 4.17 Variations of the amount of IPA in the reservoir with time during the 30%, 60% and 90% tests.

Since the IPA was not completely diluted until the last stage of a motion (i.e., last 3.0 s in the motion), its concentration was assumed to be above 31 v_2 % in most of the motion. Therefore, the value of γ_l was conservatively estimated as 29.4 mN/m on average. As indicated in Sub-section 4.4.1.1, the value of *w* was 12.7 mm. Accordingly, by equation (15), F_2 was 551 μN, much larger than the estimated

upper limit of F_1 Hence, the effect of F_1 on propulsion was neglected in this work, and the second factor was considered to be the dominant one in a motion of the ORB. The same analysis and conclusions also apply to the case of the mm-scaled SU-8 boats used in our previous work [23, 58].

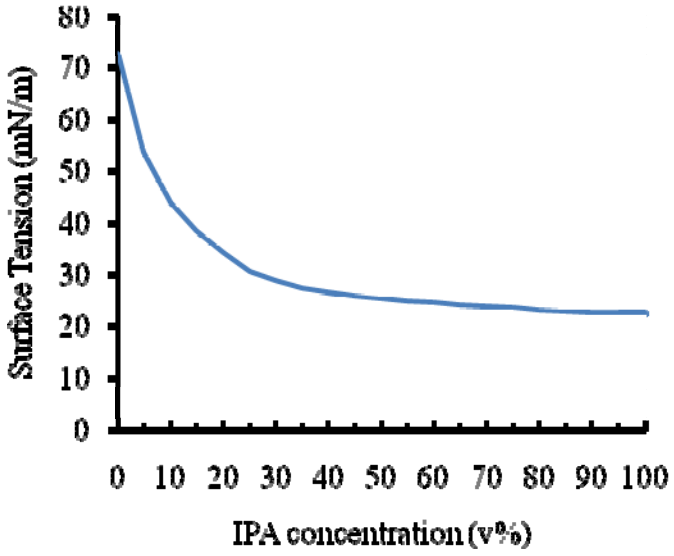

Figure 4.18 Relationship of surface tension with IPA concentration.

A simple model was further proposed to extract resistance coefficients and propulsive forces. The equation of motion along the channel direction was

$$ma = -\frac{1}{2}\rho C_\rho A V^2 + F_2, \tag{16}$$

where m denoted the total mass of the boat and IPA at time t, a acceleration of the ORB, C_ρ resistance coefficient, ρ mass density of water, V speed and A wetted surface area of the boat. In this equation, $\frac{1}{2}\rho C_\rho A V^2$ represented total resistance force [52], including viscous resistance and wave-making resistance. The value of ρ was 1 g/cm^3. During a motion, the ORB was almost completely submerged in water, whose top surface was just above the water level in the channel. The corresponding value of A was 589 mm^2. The maximum mass of the dyed IPA was 0.13 g when the reservoir was fully filled. The mass of the boat was 1.28 g, which was 10 times as large as that of the dyed IPA. The density of the dyed IPA was measured to be 0.77 g/cm^3, which was in the same order as that of water. During a motion,

as the dyed IPA flowed out, water flowed into the reservoir and filled the empty space generated due to the loss of the dyed IPA. Thus, the loss of IPA during the motion had negligible effect on the total mass. Accordingly, the total mass was considered as a constant of 1.41 g. When *V* reaches the maximum value, *a* equals zero. In-situ observation of the ORB in each test showed that, at the corresponding time instant (between *t*=1.0 s and *t*=2.0 s in the three tests), the IPA was not much diluted and *w* equaled the width of the boat. The volume concentration of the IPA in its dyed solution was measured to be 89 v_2 %. According to Fig. 6, the corresponding surface tension was 23.1 mN/m. Thus, the propulsive force also reached its maximum value of 631 μN at this time instant. By equation (16), we had

$$C_\rho = \frac{2F_{2\max}}{\rho A V_{\max}^2}. \tag{17}$$

The highest speeds of the ORB in the 90%, 60% and 30% tests were close. They were 8.5 cm/s, 8.4 cm/s and 7.8 cm/s, respectively. These three values were selected as the values of $V_{\max}$ in the corresponding tests. By equation (17), the values of C_ρ were measured to be 0.36, 0.30 and 0.30 for the 30%, 60% and 90% tests, respectively. In our previous work [23], F_2 was assumed to be constant during the entire motion of a SU-8 boat. In this work, we only assumed that F_2 was constant and equaled to the maximum value of 631 μN from the beginning of the motion to the time instant when the ORB reached the maximum speed, and determined the change of F_2 with time afterwards according to equation (16). The values of *V* and *a* in this equation were experimentally determined (Fig. 4.14). Figure 7 shows the obtained relationship of F_2 with time. As observed from this figure, the propulsive force decreased with time during the motion for each test after the time instant when the ORB reached the maximum speed. Generally, F_2 in the 90% test was close to that in the 60% test, but relatively larger than that in the 30% test, particularly in the second half of the motion. By equation (15), F_2 is related to γ_w, γ_l and *w*. Since γ_w and *w* did not change during the motion of the ORB, the change in F_2 was induced by the variation of γ_l. After the relationship of F_2 with time was determined (Fig. 4.20), we could find the relationship of

γ_l with time according to equation (15). Subsequently, based on the change of surface tension with the IPA concentration given in Fig. 4.19, we further found the variation of the IPA concentration with time (Fig. 4.21) [71]. Similar to the change of F_2 with time (Fig. 4.20), the IPA concentration decreased with time.

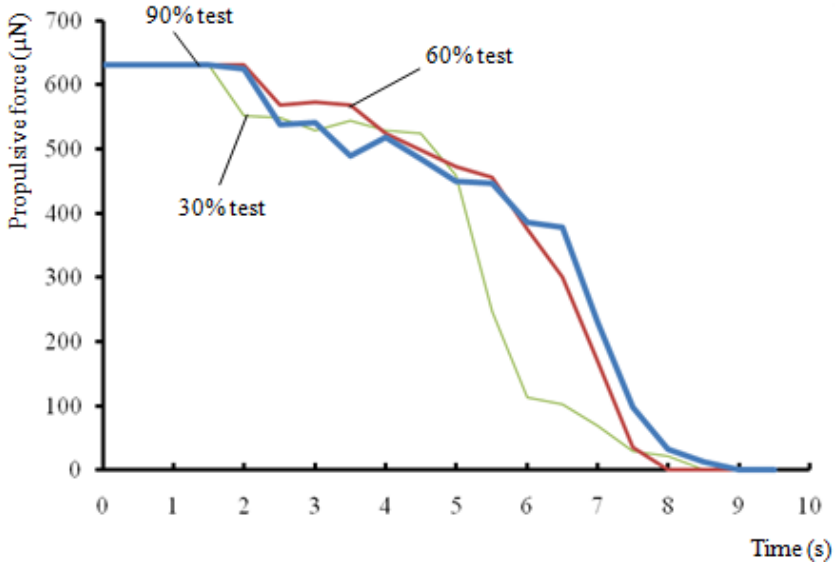

Figure 4.19 Force-time relationships of the ORB during the 30%, 60% and 90% tests.

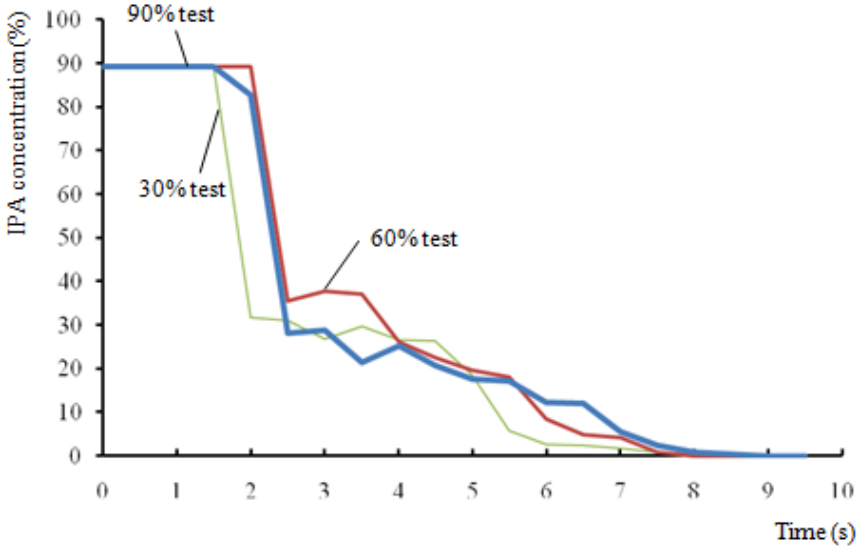

Figure 4.20 Change of the IPA concentration with time in the case of the ORB during the 30%, 60% and 90% tests.

As expected, at different time instants, generally the IPA concentrations in the 60% and 90% tests were close but relatively larger than that in the 30% test. As observed from the three types of tests (Fig. 4.14),

the color of the IPA became lighter during a motion, implying that the IPA concentration in the reservoir gradually decreased with time. Accordingly, the difference in the surface tensions of water and IPA also decreased with time, and thus F_2 also decreased with time. As also seen from Fig. 4.18, at a particular time instant, the amount of IPA in the reservoir in the 90% test was always higher than those in the 60% and 30% tests, while that in the 60% test was higher than that in the 30% test. The IPA in the reservoir was diluted by water due to binary diffusion. The degree of dilution should decrease with the increasing amount of the IPA. Therefore, the IPA concentration in the reservoir at a particular instant should be the highest in the 90% test, and lowest in the 30% test. Accordingly, generally F_2 had the largest value in the 90% test and the smallest one in the 30% test. In the second half of each test, the IPA concentration was below 25 v_2 % (Fig. 4.21). As observed from Fig. 4.19, when the IPA concentration was below 25 v_2 %, a slight variation in the concentration induced a relatively large change in the surface tension of the IPA. Accordingly, the higher IPA concentrations in the 60% and 90% tests made the corresponding propulsive forces relatively larger than that in the 30% test during the second half of the motion.

4.4.2 Results of the CRB

The CRB case was much complicated than the ORB. We examined the 15%, 30%, 45%, 60%, 75% and 90% tests of CRB. Air bubble was trapped in the reservoir for 15%, 30% and 45% test. Air bubble might or might not be trapped in the reservoir for the 60% test. Air bubble was not observed in the reservoir for 75% and 90% tests. It implied that the IPA loading below 60% might generate air bubble in the reservoir. However, there was no bubble in the ORB case. Therefore, four types of tests- 30% test with bubble, 60% test with bubble, 60% test without bubble and 90% test without bubble- were selected to explore the exchange mechanism between IPA and water in the CRB reservoir. For simplification, the previous tests will be called 30% bubble test, 60% bubble test, 60% test and 90% test, respectively.

4.4.2.1 Exchange processes of water and IPA

The exchange process of water and dyed IPA was more complicated in the case of the CRB, since the top surface of the reservoir was sealed. This exchange process varied dramatically with the amount of the IPA loaded into the reservoir. Figure 4.22 shows the exchange process of water and IPA in the reservoirs of the CRB.

In the 90% test, the exchange process included two basic stages. In the first stage, the IPA and water flowed in a manner similar to what was observed in the case of the ORB (Fig. 4.22(a)). The second stage included two steps (Figs. 4.22(b), 4.22(c), 4.22(m) - 4.22(o)). In the first step, the continuous flow of IPA from the nozzle caused more water to get into the reservoir (Fig. 4.22(m)). The water eventually blocked the nozzle, and sealed the IPA inside the reservoir (Fig. 14.22(n))). In the second step, the difference between the densities of water and dyed IPA decreased the inclined level of the IPA/water interface inside the reservoir. In the meantime, IPA flowed toward the nozzle of the reservoir (Fig. 4.22(o)). These two steps in the second stage alternated until the color of the dyed IPA became very light (i.e., IPA was much diluted in the reservoir). The oscillating shift of these two steps generated a gurgling-like motion, i.e. approximately periodic movement of acceleration and deceleration. This repeated phenomenon of deceleration and acceleration is similar to what is observed when water flows out from a bottle. When one holds a water-filled bottle upside down, the water slows down and speeds up in a relatively periodic manner. As water flows out of the bottle, the empty space within the bottle increases, and air pressure over there decreases and becomes lower than the atmospheric pressure. The increase of this pressure difference slows down the water flow. As more air enters the bottle, this pressure difference reduces, making water flow faster. Bassik et al. also found Gurgling-like phenomena in the motions of gels [38]. They believed that these phenomena were induced by an oscillating shift between the collapse and rehydration of the gels.

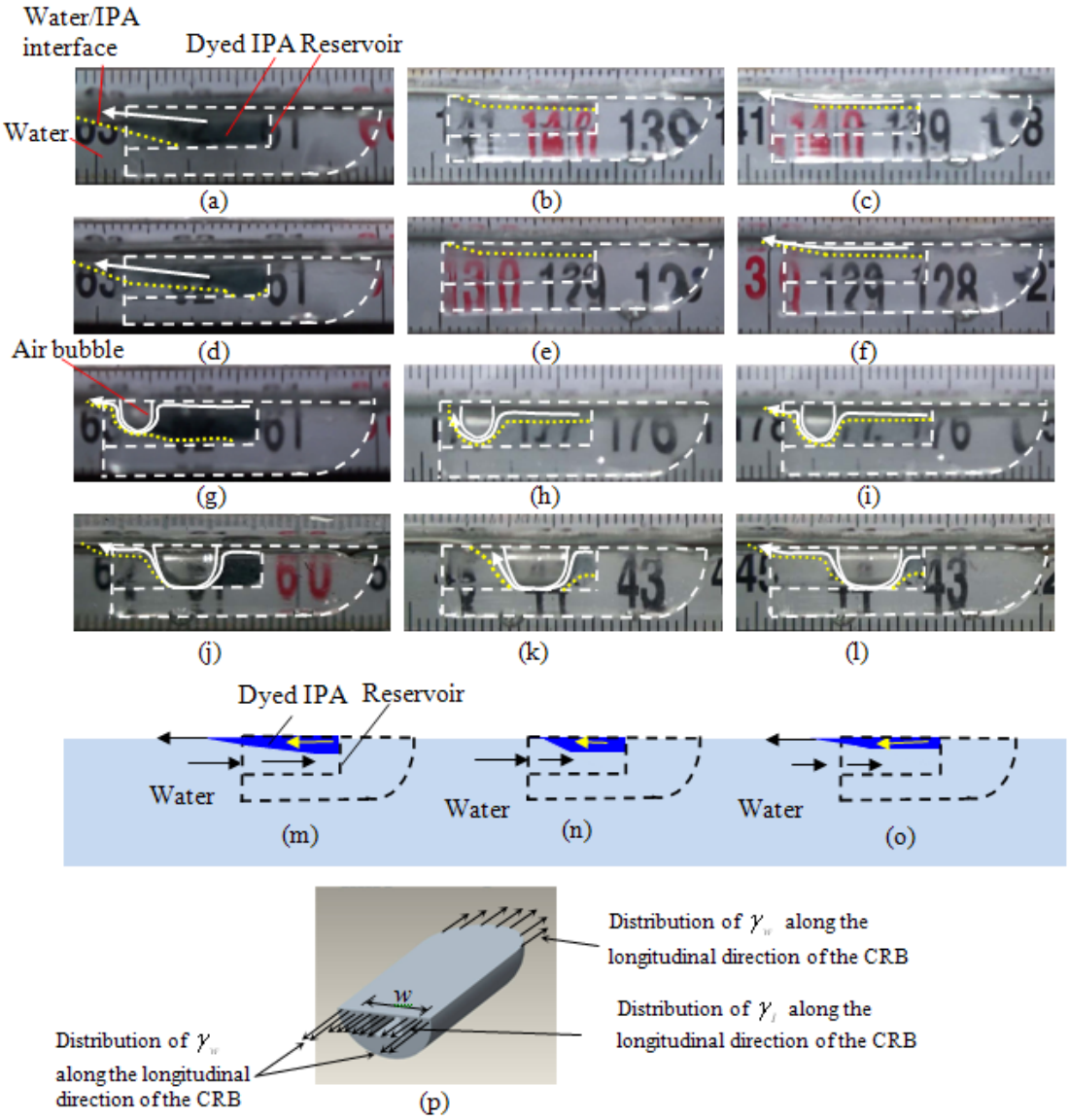

Figure 4.21 In-situ observation of the exchange processes of water and IPA in the reservoirs of the CRB (side views). 90% test: (a) IPA flowed out of the nozzle (*t*=0.2 s), (b) IPA was blocked inside the reservoir by water (*t* =58.5 s), and (c) IPA flowed out of the nozzle again (*t*=61.4 s). 60% test: (d) IPA flowed out of the nozzle (*t*=0.1 s), (e) IPA was blocked inside the reservoir by water (*t* =85.7 s), and (f) IPA flowed out of the nozzle again (*t*=87.7 s). 60% bubble test: (g) IPA flowed out of the nozzle (*t*=0.1 s), (h) IPA was blocked inside the reservoir by water (*t* =127.5 s), and (i) IPA flowed out of the nozzle again (*t*=129.5 s). 30% bubble test: (j) IPA flowed out of the nozzle (*t*=0.5 s), (k) IPA was blocked inside the reservoir by water (*t* =223.0 s), and (l) IPA flowed out of the nozzle again (*t*=225.5 s). (m-o) Illustration of the exchange process of water and IPA in the reservoir of the CRB (side views). (p) Distribution of fore-and-aft surface tensions along the longitudinal direction of the CRB.

Distributions of fore-and-aft surface tensions along the longitudinal direction of the CRB were illustrated in Fig. 4.22(p). Since the reservoir of the CRB had a ceiling, the aft surface tension remained to be that of water before the exit of the IPA from the reservoir, and there was no difference in the fore-and-aft surface tensions. On the other hand, the reservoir of the ORB had a top opening, and the IPA inside this reservoir had a free top surface. As illustrated in Fig. 4.14(d), even if the IPA inside the reservoir of the ORB did not exit the reservoir, it changed the aft surface tension. Following the line of reasoning used in Sub-section 3.3, it could be readily shown that the propulsive force in the case of the CRB was also mainly induced by the difference between the fore-and-aft surface tensions. Equation (15) applied as well to the case of the CRB. In the first stage of the exchange process, the speed kept increasing until the driving force was balanced by water resistance. After water had blocked the nozzle in the first step of the second stage, the propulsive force was zero, and the CRB slowed down due to water resistance. As the IPA started moving out of the nozzle in the second step, the difference between the fore-and-aft surface tensions generated a propulsive force, and subsequently the CRB sped up. The 60% test had a similar IPA-water exchange process, which also included two basic stages. The corresponding exchange process was shown in Figs. 4.22(d) - 4.22(f).

The exchange process in the 60% bubble test included two basic stages as well. In the first stage, an air bubble formed inside the reservoir as water flowed into the reservoir (Fig. 4.22(g)). Since the density of air was lower than those of both water and IPA, the bubble was against the ceiling of the reservoir. However, this bubble was not large enough to block the entire cross-section of the reservoir. The flowing directions of water and IPA in the first stage of the exchange process were illustrated in Fig. 4.22(g). The water first moved into the reservoir through the nozzle and then continued to get into the inner part of the reservoir via the gap between the bubble and the bottom of the reservoir. In the 60% test, the IPA always flowed from the inner portion of the reservoir towards the nozzle along the ceiling of the reservoir. However, in the 60% bubble test, the IPA first moved along the bottom surface of the bubble and then along the ceiling of the reservoir. As the IPA moved along the bottom surface of the bubble, due to binary diffusion between the IPA and the underneath water, the concentration of the IPA along the

bottom surface of the bubble gradually decreased towards the nozzle, and a gradient of surface tension was created accordingly. This gradient made the IPA keep moving from the inner portion to the outer portion of the reservoir along the bottom surface of the bubble. Thus, the IPA was not blocked at the gap by water during the entire exchange process. On the other hand, in the 60% bubble test, the exchange process of water and IPA in the outer portion of reservoir (i.e., on the left-hand side of the bubble, as shown in Fig. 4.22(g)) was similar to what was observed in the first stage of the 60% test. In the second stage, the blocking and unblocking phenomena also occurred at the nozzle of the reservoir (Figs. 4.22(h) and 4.22(i)). As these phenomena repeated, gurgling-like movements were observed.

The size of the trapped bubble increased with the decreasing amount of loaded IPA. When 30% of the reservoir was filled by the IPA, a bubble, which was larger than that in the 60% bubble test, was generated during the corresponding motion of the CRB. This bubble blocked most of the cross-section of the reservoir. On the other hand, as shown in Figs. 4.22(j)- 4.22(l), the 30% bubble test still had a similar IPA-water exchange process as the 60% bubble test.

4.4.2.2 Speed-time relationships

Figure 22 gives speed-time relationships for the case of the CRB. In comparison with the case of the ORB (Fig. 4.15), four points could be observed from these relationships.

First, the highest speeds of the CRB in the 90%, 60%, 60% bubble and 30% bubble tests were 7.1 cm/s, 7.0 cm/s, 1.8 cm/s and 1.6 cm/s, respectively. They were lower than their counterparts in the ORB tests. The highest speeds of the ORB in the 90%, 60% and 30% tests were 8.5 cm/s, 8.4 cm/s and 7.8 cm/s, respectively. The translational speeds of mm-scaled, disk-shaped polymer gels were reported to have an order of 1 cm/s [35,36], while those of mm-scaled, rectangular-shaped polymer gels had an order of 10 cm/s [38]. The mm-scaled SU-8 boats [23,58], experienced the same order of speeds as the rectangular-shaped polymer gels, while the ORB and CRB had the same order of speeds as the disk-shaped polymer gels. The differences in the highest speeds of the CRB and ORB were caused by the corresponding differences in the propulsive forces and resistance coefficients. As will be indicated in next sub-section, the largest propulsive forces in the 90% and 60% tests of the CRB were the same as the

counterparts in the 90% and 60% tests of the ORB. However, the CRB suffered higher water resistances than the ORB, since the determined values of C_ρ were larger in the case of the CRB. In the bubble tests of the CRB, the largest propulsive forces were much smaller than their counterparts in the corresponding tests of the ORB.

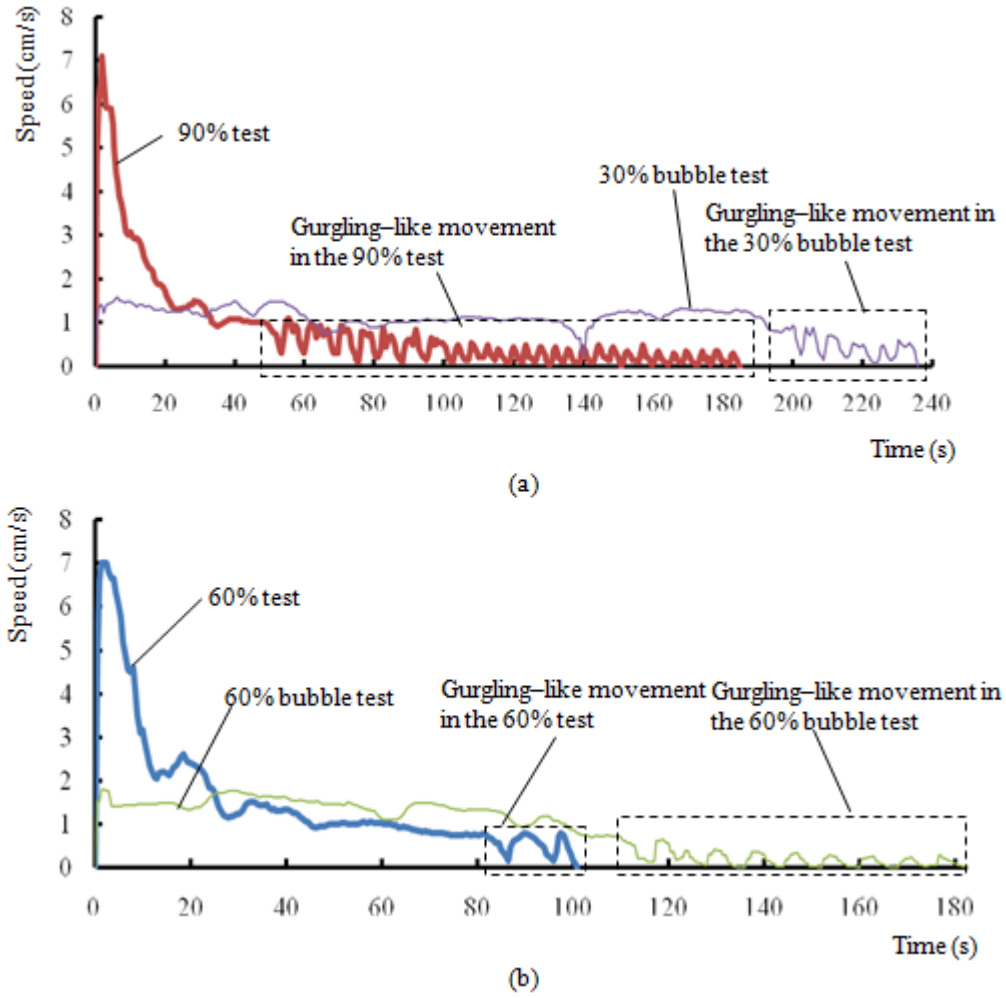

Figure 4.22 Speed-time relationships of CRB under different test conditions. (a) Speed-time relationships in the 30% bubble and 90% tests of the CRB. (b) Speed-time relationships in the 60% test of the ORB, 60% bubble test of the CRB and 60% test of the CRB.

Second, at the beginning of the motion (i.e., 0-12 s), the speed-time curves of the CRB were similar with those of the ORB. That is, both boats first rapidly increased and then quickly decreased their speeds. However, the CRB had different speed-time curves in the 60% bubble and 30% bubble tests. In

either test, the speed first increased and then did not have much change for a relatively long period until the gurgling-like phenomenon appeared.

Third, the total travel periods of the CRB in 90%, 60%, 60% bubble and 30% bubble tests were 185 s, 101 s, 183 s and 236 s, respectively, while those of the ORB in the 90%, 60% and 30% tests were 9.5 s, 9 s and 9 s. The CRB had a longer travel time than the ORB for the same IPA loading. In addition, the total travel distances of the CRB in the 90%, 60%, 60% bubble and 30% bubble tests were experimentally determined to be 157.4 cm, 157.3 cm, 320.9 cm, and 245.9 cm, respectively. They were also much longer than their counterparts in the ORB tests. The total travel distances of the ORB in the 90%, 60% and 30% tests were 57.9 cm, 55.1 cm and 46.8 cm, respectively. Furthermore, when a bubble was trapped in the reservoir, the CRB experienced longer travel time and distance than in the case that the reservoir did not have any bubbles. For example, the travel distance of the CRB in the 60% bubble test was 320.9 cm, which was 2.0 times that of the CRB in the 60% test (157.3 cm) and 5.8 times that of the ORB in the 60% test (55.1 cm). In addition, the travel time and distance in the 30% bubble test were both longer than those in the 60% bubble test.

Two factors may contribute to the similarities and differences indicated in the second and third points: reservoir structures, and presence of bubbles. In the case of the ORB, the top of the reservoir was open. Accordingly, the IPA had a free top surface, and did not suffer any constraint from the top when it flowed inside the reservoir along the horizontal direction. However, in the case of the CRB, the reservoir had a ceiling, which made the flow speed of the IPA become zero at its top surface (relative to the ceiling) and consequently slowed down the movement of the IPA in the reservoir. Thus, during the existing process, the flowing rate of the IPA in the case of the ORB was higher than that in the case of the CRB. When both boats were loaded with the same amount of the IPA, the IPA existed longer inside the CRB, making the travel time and distance both longer than in the case of the ORB. When there was a bubble in the reservoir of the CRB, the flow rate of the IPA was reduced compared with the case that no bubble was trapped inside the reservoir. Part of the cross-section of the reservoir was blocked by the bubble, slowing down the movement of the IPA inside the reservoir. The bubble in the 60% bubble test was larger

than that in the 30% bubble test. Accordingly, a larger portion of the cross-section of the reservoir was blocked by the corresponding bubble in the 30% bubble test, making the IPA flow more slowly inside the reservoir.

Fourth, the CRB experienced a gurgling-like movement at the end of each test. However, no gurgling-like phenomenon was observed in any test of the ORB. This difference was also induced by the difference in the reservoir structures. As illustrated in Fig. 21(m) - Fig. 21(o), the gurgling-like movement occurred in the case of the CRB due to the sealing of the IPA inside the reservoir. This sealing made the boat lose its propulsive force. In the case of the ORB, the IPA in the reservoir had a free top surface. There existed IPA beside the inner sidewall of the reservoir until water completely occupied the reservoir. The difference between the surface tension of this portion of IPA and that of water in front of the boat still provided the propulsive force to drive the boat forwards (Fig. 14(j)), even if the IPA was blocked inside the reservoir by water. Hence, the gurgling-like phenomena did not occur in the case of the ORB.

In addition, it can also be observed from Fig. 4.22 that, before the occurrence of gurgling-like behaviors, there existed local fluctuations of speeds. They were induced by the collisions of the CRB with the channel sidewalls. The CRB was not perfectly symmetric with respect to its middle line. This may cause the collision of the CBR with the channel sidewalls during a motion. After a collision, the CRB first decreased its speed and then gradually increased its speed until the occurrence of next collision. The same applied to the ORB. The local fluctuations of speeds induced, respectively, by the collisions and the blockage of the nozzle by water could be distinguished through side view of the exchange process of water and IPA in the reservoir or via top view of the movements of the CRB.

4.4.2.3 Propulsive forces

We first determined the values of C_ρ for the 60% and 90% tests. In either test, the entire stern was covered by IPA, and the IPA was not much diluted. As what was done in the case of the ORB, we assume that the propulsive force equaled 631 μN from the beginning of the motion to the moment that the CRB had the highest speed. The determined values of C_p for both tests were 0.43, larger than those in

the three types of ORB tests. We then determined the change of F_2 with time according to equation (16). The values of V and a in this equation were experimentally determined (Fig. 4.22).

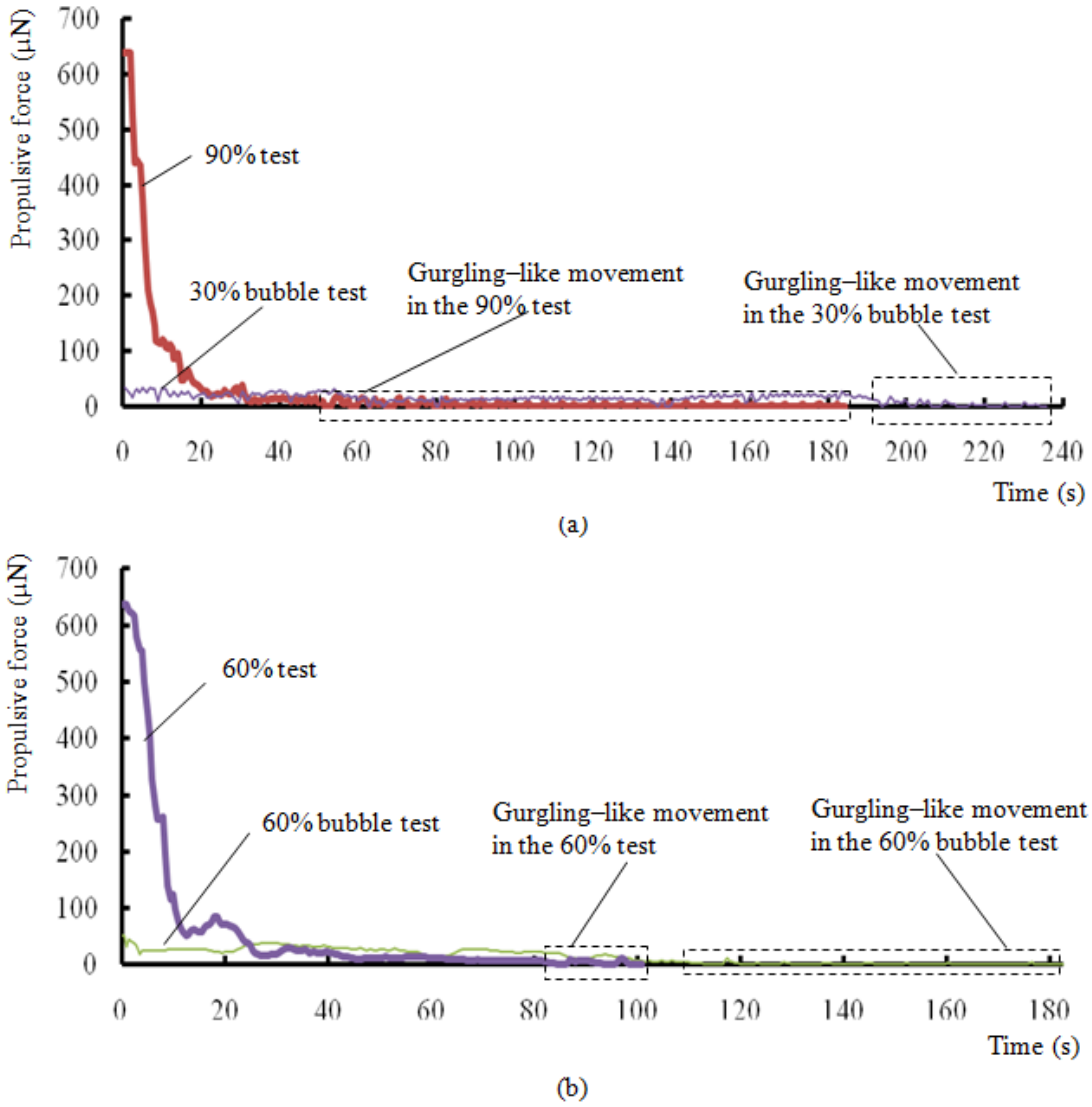

Figure 4.23 Force-time relationships of the CRB under different test conditions. (a) in the 30% bubble and 90% tests, as well as (b) in the 60% bubble and 60% tests.

Figure 4.23 shows the obtained relationship of F_2 with time. In the 90% test, the force promptly decreased from the highest value of 631 μN at 2 s first to 65.8 μN at 15 s and then to 17.6 μN at 32 s. After that, it oscillated between 0 and 17.6 μN for a long time (from 32 s to 185 s) (Fig. 4.23(a)). In the 60% test, F_2 changed with time in a similar manner ((Fig. 4.23(b)). The rapid changes in the propulsive

forces at the beginnings of the 60% and 90% CRB tests were similar to those in the corresponding ORB tests. In either of the 30% and 60% bubble tests, due to small flow rate of the IPA, it did not cover the entire stern from the beginning of the motion. Accordingly, the largest propulsive forces in these two tests were smaller than their counterparts in the corresponding CRB tests of no bubbles. Subsequently, we did not assume that the propulsive force equaled 631 μN at the beginning of the motion, and the C_p of the 60% and 90% tests was used for that of the 30% and 60% bubble tests. Based on these and experimentally obtained V and a (Fig. 4.22), we calculated the propulsive forces for these two tests involving bubbles (Fig. 4.23). In the 30% bubble test, the propulsive force was around 17 μN before the occurrence of the gurgling-like movement at t=200 s. After that, this force varied between 0 and 15 μN. In the 60% bubble test, the propulsive force was around 24 μN before the occurrence of the gurgling-like movement at t=110 s. Subsequently, this force changed between 0 and 12 μN. Since the loaded IPA was consumed more slowly in these two bubble tests than in the 60% and 90% CRB tests, the corresponding IPA concentration had smaller changes for the most time of the motions. Therefore, the changes in the propulsive forces of the 30% and 60% bubble tests were not as dramatic as their counterparts in the 60% and 90% CRB tests.

In either of the 60% and 90% CRB tests, when gurgling-like phenomena occurred, there was not enough IPA flowing out the nozzle to cover the entire stern. In addition, in either of the 30% bubble and 60% bubble tests, the IPA did not cover entire stern from the beginning of the motion. The incomplete coverage of the stern made it difficult to precisely determine the corresponding value of w. Therefore, we did not consider the change of the IPA concentration with time in the case of the CRB.

CHAPTER 5

CONCLUSIONS

5.1 Miniaturized Boats

5.1.1 Test in Straight Channels

In this section first we try to address the questions raised in section 1.2 -“State of problem”. The answers will be arranged in three parts- questions related to 1) miniaturized SU-8 boat, 2) miniaturized SU-8 flotilla and 3) miniaturized PDMS flotilla. Finally we will summarize and discuss our future work.

It is discovered that both water depth and channel width had strong influence on the miniaturized flotilla’s motion. The average propulsive force should decrease with the increasing time as the boat progresses. In addition, the propulsive force in the three types of tests was hardly related to the total amount of water in the channel during these tests

Since 9.4-mm tests had the largest resistance coefficient amount the three types of test, it was expected that, for a particular amount of load IPA, miniaturized boat should have longer travel distance in the other two types of tests than in 9.4-mm tests.

5.1.2 Magnetic Stoppage

Before the boat passes the permanent magnet, since the magnetic force in the horizontal direction adds to the propulsion force F, the acceleration increases, which means the velocity remains positive, so the boat keeps moving in the original direction.

After the boat passes the permanent magnet, since the magnetic force in the horizontal direction is in the opposite direction to the propulsion force F, the acceleration decreases. If the

magnetic force is large enough, the acceleration could reduce to zero even negative, thereby reducing the boat's speed till it stops, which is our objective.

5.2 Miniaturized Flotillas

5.2.1 Test in Straight Channels

The miniaturized flotilla moved in a straight channel like a rigid object. Collisions were not observed between neighboring miniaturized boats (Fig. 4.7). The portion of the Nylon wire between two neighboring miniaturized boats, as well as the whole miniaturized flotilla, remained straight.

The test results qualitatively agreed with those obtained from the simple analysis in Section 2.3. That is, the largest propulsive force would be generated when the fifth miniaturized boat was actuated. As such, this miniaturized boat was chosen as the locomotive of the corresponding miniaturized flotilla in subsequent tests. On the other hand, it was not clear why there was much difference in the travel distances and average speeds when the first four miniaturized boats were each individually actuated. This might be caused by the different moving paths of the IPA after it exited those miniaturized boats, which could result in much difference in propulsive forces, water resistances and vertical orientations of the miniaturized boats.

Both water depth and channel width had strong influence on the miniaturized flotilla's motion. In addition, the average speed of the miniaturized flotilla in each type of tests increased with the increasing channel width when the water levels were the same.

The increase of resistance due to the decrease of water depth was so-called shallow-water effect [53]. The total resistance includes viscous resistance and wave-making resistance [52]. Both increase with the decreasing water depth. According to the conservation law of mass, if the miniaturized flotilla is considered as being at rest in a flowing stream, the water passing below it in shallow water must speed up more than in deep water. Accordingly, the viscous resistance increases due to the increase of the velocity gradient (the viscous resistance is linearly proportional to this gradient); also, the wave pattern around the miniaturized flotilla changes during transition of the test from deep to shallow water [44]. The

amplitude of the wave increases with the decreasing water depth. As such, wave-making resistance also increases with the decreasing water depth. Likewise, the reduction of a channel width further increases both viscous and wave-making resistances [54].

Both water depths and channel widths had much influence on the flotilla's motions. The average speed of the miniaturized flotilla increased with the increasing water depth in each channel.

These results indicated that the water resistance increased with the decreasing water depth and channel width. On the other hand, compared with channel width, water depth appeared to have a larger effect on the motion of a miniaturized flotilla.

The average speed in the performed tests varied from 65.3 mm/s to 177.8 mm/s. They were lower than the average speed of a single miniaturized boat tested in a trapezoidal channel, which varied from 150 mm/s to 300 mm/s. Naturally, this difference in the average speed was due to the fact that the miniaturized boat suffered a smaller water resistance. The water resistance was linearly proportional to both the resistance coefficient and the wetted area of a floating object.

It is expected that the different wetted areas between the miniaturized boats and flotillas should also cause a large difference in their water resistance. The miniaturized flotilla consisted of five miniaturized boats; however, both miniaturized boats and flotillas were almost completely submerged in the water, as observed from their relationship to the water surface. Moreover, the PDMS connectors were wetted. Thus, the wetted area of the miniaturized flotilla was at least five times as large as that of an individual miniaturized boat, causing much difference between their resistances.

5.2.2 Test in Circular Channels

Similar to the motions in the straight channels, the miniaturized flotilla moved in the circular channel like a rigid object (Fig. 4.9). Collision was not observed between neighboring boats. A centripetal force is needed for generating radial motion of an object.

The travel distance and the moving speed of the miniaturized flotilla in the circular channel indicated that the water resistance also increased with the decreasing water depth in the circular motions.

5.3 Gurgling-like Effect

Based on this observation and force analysis of ORB and CRB tests, we interpreted driving mechanisms of the two boats. Three factors mainly affected the exchange process between the IPA and water in the case of the ORB: difference between surface tensions of water and IPA, a free convection flow due to gravity, and binary diffusion between the IPA and water. However, in the case of the CRB, in addition to these three factors, another two factors might also affect the exchange process: the ceiling of the reservoir, and the presence of a bubble. These two factors made the exchange processes different in the two boats. In the case of the ORB, the top of the reservoir was open. The flow of the IPA inside the reservoir along the horizontal direction did not suffer any constraint from the top. Accordingly, the IPA was continually drawn away from the reservoir by water. However, in the case of the CRB, the reservoir had a ceiling, which slowed down the flow of the IPA inside the reservoir. Thus, the flowing rate of the IPA at the reservoir nozzle in the case of the ORB was higher than that in the case of the CRB. The IPA was consumed in a much longer time in the case of the CRB. Consequently, both travel distance and time of the CRB were longer those of ORB, while the average speeds of the ORB were larger than those of the CRB. When there was a bubble in the reservoir of the CRB, the flowing rate of the IPA was further reduced compared with the case that there was no bubble. Hence, both travel distance and time in the former case were longer than those in the latter case. According to these results, in the real applications of solvent-driven miniaturized boats, in order to have a long travel distance, the CRB is preferred, which has a bubble trapped in its reservoir. On the other hand, to have a high speed, the ORB should be selected.

In addition, based on observed exiting processes of the IPA and experimentally determined speed-time relationships, we also set up a simple model to find the variations of propulsive forces for the ORB and CRB, and determined the changes of the IPA concentration with time in the case of the ORB.

Furthermore, we investigated the exiting process when the reservoir of the ORB was shallow. We found that, depending on the values of the height difference, h, between the bottom of the reservoir and the water surface outside the reservoir, three different phenomena might appear: (I) if $h \leq 1.3$ mm, then the reservoir was empty at the end of the test and no water flowed into the reservoir during the test; (II) if 1.3 mm$<h \leq 2.3$ mm, then the reservoir was empty at the end of the test while water flowed into the reservoir during the test; and (III) if 2.3 mm$<h \leq 3$ mm, then the reservoir was filled by water at the end of the test. The difference in the filling results was induced by the interplay among Magrangoni effect, free convection, and recovery of a hollow spot by surrounding water. The corresponding findings interpreted the exiting process of the IPA observed in the open reservoir of a mm-scaled SU-8 boat that we have previously developed, and also explained the filling result in the open reservoir of the ORB.

APPENDIX A

LIST OF PUBLICATIONS

1. Propulsion of Microboats using Isopropyl Alcohol as a Propellant, Luo, Cheng; Li, Hao; Liu, Xinchuan, *Journal of Micromechanics and Microengineering*, Volume 18, Issue 6, pp. 067002 (2008).

2. Dramatic squat and trim phenomena of mm-scaled SU-8 boats Induced by Marangoni effect, Cheng Luo. Lei Qiao . Hao Li, *Microfluid Nanofluid* ,Volume 9, Issue 2 (2010), Page 573.

3. Driving Mechanisms of CM-Scaled PDMS Boats of Respective Close and Open Reservoirs, Xinchuan Liu, Hao Li , Lei Qiao and Cheng Luo, *Langmuir* (in review).

4. Theoretical and numerical studies of new suspended-silicon-nanowire based static sensors, Hao Li; Xinchuan Liu; Cheng Luo, *Proc. SPIE*, Vol. 6223, 62230Q (2006).

5. Deflection of silicon dioxide microbridge under distributed load, Hao Li, Anirban Chakraborty, Xinchuan Liu, Hui Wang, and Cheng Luo, *Proc. SPIE*, Vol. 6556, 655608 (2007).

6. Generation of Silicon Nanowires Using a New Thinning and Trimming Method, Hui Wang, Anirban Chakrabortya, Xinchuan Liua, Hao Lia, Cheng Luo, *Proc. SPIE*, Vol. 6556, 65561P (2007).

7. Development of a Self-propelled, Miniaturized PDMS Flotilla (in preparation).

8. Development of a Self-propelled Water Microtrain (in preparation).

REFERENCES

1. Tang W C, Nguyen T-C H and Howe R T 1989 Laterally Driven Polysilicon Resonant *Microstructures Sensors and Actuators* 20 25.

2. Fan L-S, Tai Y-C and Muller R S 1989 IC-processed Electrostatic Micromotors *Sensors and Actuators* 20 41.

3. Fearing R S, Chiang K H, Dickinson M, Pick D L, Sitti M and Yan J 2000 Wing transmission for a micromechanical flying insect, *IEEE Int. Conf. Robotics and Automation* (San Francisco) pp 1509–16.

4. R.A. Day, J.D. Gelorme, D.A. Russell, S.J. Witt, US-5304457, 1994.

5. M. Mauger, A. Dubault, J.L. Halary, Synthesis and Physico-chemical Characterization of Networks Based on Methacryloxypropyl-grafted Nano-silica and Methyl Methacrylate**,** *Polymer International* 53 378.

6. H.K. Kim, J.G. Kim, J.D. Cho, J.W. Hong, Optimization and Characterization of UV-curable Adhesives for Optical Communications by Response Surface Methodology, P*olymer Testing* 22 899.

7. Alvaro Mata, Aaron J Fleischman and Shuvo, Fabrication of Multi-layer SU-8 Microstructures, *Journal of Micromechenical Microengineering 16* 276–284.

8. Saghiri, A. A. Kaden, M. Rossler, K. Wijnaendts, R. Preuss, S. Forozan, A. SU 8 Multiple Layer Structuring by Means of Maskless Photolithography, *Proceedings-SPIE the International Society for Optical Engineering 2006*, Volume 6110, pages 611003.

9. Bohl, Benjamin; Steger, Reinhard; Zengerle, Roland; Koltay, Peter, Multi-layer SU-8 Lift-off Technology for Microfluidic Devices, *Journal of Micromechanics and Microengineering*, Volume 15, Number 6, June 2005 , pp. 1125-1130.

10. Roch, I., Fabrication and Characterization of An SU-8 Gripper Actuated by a Shape Memory Alloy Thin Film, *Institute of Physics*, Volume. 13, Issue 2, pg. 330, 2003.

11. Jo, L.M. Van Lerberghe, K.M. Motsegood, and D.J. Beebe, Three-dimensional Mcro-channel Fabrication in Polydimethylsiloxane (PDMS) Elastomer, *Journal of Microelectromechanical Systems* 9, 76–81.

12. A. Mata, C. Boehm, A.J. Fleischman, G. Muschler, and S. Roy, Growth of Connective

13. Tissue Progenitor Cells on Microtextured Polydimethylsiloxane Surfaces, *Journal of Biomedical Materials Research* 62, 499–506.

14. M.A. Unger, H.-P.Chou, T. Thorsen, A. Scherer, and S.R. Quake, Monolithic Microfabricated Valves and Pumps by Multilayer Soft Lithography, *Science* 288, 113–116.

15. J.M.K. Ng, I. Gitlin, A.D. Stroock, and G.M. Whitesides, Components for Integrated Poly(dimethylsiloxane) Microfluidic Systems ,*Electrophoresis* 23, 3461–3473.

16. Y. Xia and G.M. Whitesides, Soft Lithography, *Angewandte Chemie International Edition* 37, 550–575.

17. Mark J., *Polymer Data Handbook*, Oxford Univ. Press, New York.

18. Jo, B-H et al, 2000, Three-Dimensional Micro-Channel Fabrication in Polydimethylsiloxane (PDMS) Elastomer, *Journal of Microelectromechanical Systems* 9 76-81.

19. Rabih Zaouk, Benjamin Y. Park and Marc J. Madou, Fabrication of Polydimethylsiloxane Microfluidics Using SU-8 Molds, Microfluidic Techniques Reviews and Protocols, Humana Press, 2006.

20. Westwood, S. M.; Jaffer, S.; Gray, B. L. Enclosed SU-8 and PDMS Microchannels with Integrated Interconnects for Chip-to-chip and World-to-chip Connections, *Journal of Micromechanics and Microengineering*, Volume 18, Issue 6, pp. 064014.

21. Thomson J, On Certain Curious Motions Observable on the Surfaces of Wine and Other Alcoholic Liquors. *Philosophy Magzine* 10:330–359.

22. Scriven LE, Sternling CV (1960) The Marangoni Effects. *Nature* 167:186–188.

23. Li H, Luo C., Actuation, Stopping and Collection of Miniaturized boats, *18th ASME Annual Conference on Information Storage and Processing Systems,* MNT-B3, San Fransisco, June 2008.

24. Luo. C, Hao Li et al, Propulsion of Miniaturized boats and Flotillas Using Isopropyl Alcohol as a Propellant, *Journal of Micromechanical and Microengineering* 18 067002.

25. *Proceedings of the 1st IARP Workshop on Medical and Helthcare Robots*, Ottawa, Canada, pp.789-792, June 23 -24, 1988.

26. *Special session on Biorobotics, Proc. 12th IEES/EMBS Conf.*, Philadelphia, U.S.A., pp.1942-1943, November 1-4 1990.

27. T. Fukuda, Hosokai et al, "Distributed Type of Actuator by Shape Memory Alloy and its Application to Underwater Mobile Robotic Mechanism", *Proceedings of IEEE Conference on Robotics and Automation*, Volume.2, pp.1316-1332, Nara, Japan, Jan. 1991.

28. Fukuda, Kawamoto, Arai and Matsuura, "Mechanism and Swimming Experiment of Micro Mobile Robot in Water", *Proceedings of IEEE Conference on Robotics and Automation*, Volume 1, pp.814-819, San Diego, California, May 1994.

29. Fukuda, Kawamoto, Arai and Matsuura, Steering Mechanism of Underwater Micro Mobile Robot, *Proceedings of IEEE Conference on Robotics and Automation*, Volume 1, pp.363-368, Nagoya, Japan, May 1995.

30. M. Mojarrad and M. Shahinpoor, Biomimetic Robot Propulsion Using Polymeric Artificial Muscles, *Proceedings of IEEE International Conference on Robotics and Automation*, pp.2152-2157, New Mexico, USA.

31. S.Guo, T. Fukuda, N. Kato and K. Oguro, Development of Underwater Microrobot Using ICPF Actuator, *Proceedings of IEEE International Conference on Robotics and Automation*, pp.1829-1834, Leuven, Belgium.

32. Keisuke Oguro, Kinji Asaka and Hiroyasu Takenaka, Polymer Film Actuator Driven by a Low Voltage, *Proceedings of 4th International Symposium on Micro Machine and Human Science*, pp. 39-40, JAPAN.

33. Visvanathan et al.,Propulsion and Steering of A Floating Mini-robot Based on Marangoni Flow Actuation *Proceedings of IEEE International Conference on Transducers*, Denver, U.S.

34. Song, Surface-Tension-Driven Biologically Inspired Water Strider Robots: Theory and Experiments, *IEEE Transactions on Robotics*, Volume 23, No. 3.

35. Guo et al., Hybrid Type of Underwater Micro Biped Robot with Walking and Swimming Motions, *Proceedings of the IEEE International Conference on Mechatronics & Automation*, Niagara Falls, Canada.

36. Osada et al., Spontaneous Motion of Amphoteric Polymer Gels on Water, *Japanese Journal of Applied Physics* 34: L511.

37. Gong J. et al., Motion of Polymer Gels by Spreading Organic Fluid on Water, *Journal of Physical Chemistry* ,100:11092.

38. Mitsumata et al., Solvent-driven Chemical Motor, *Langmuir* 16: 307.

39. Bassik et al., Solvent Driven Motion of Lithographically Fabricated Gels, *Langmuir* 24:12158.

40. Su et al., Liquid Mixing Driven Motions of Floating Macroscopic Objects, *Applied Physics Letters*, 90:144102.

41. J. G. Smits, H. A. C. Tilmans, and t. S. J. Lammerink, Pressure Dependence of Resonant Diaphragm Pressure Sensors, Technical Digest, *3rd International conference on Solid-State Sensors and Actuators*, Philadelphia, Penn., pp. 93-96.

42. D. C. Satchell and J. C. Greenwood, Silicon microengineering for accelerometers, *Proceeding Institution Of Mechanical Engineering, volumel. 1987-2, Mechanical Technology of Inertial Devices*, Newcastle, England, pp. 191-193.

43. W. Benecke, A. Heuberger, W. Reithmuller, U. Schnakenberg, H. Wlfel-scheider, R. Kist, G. Knoll, S. Ramakrishnan, and H. Hfflin, Optical Excited Mechanical Vibrations in Micromachined Silicon Cantilever Structures, Technical Digest, *4th International conference on Solid-State Sensors and Actuators*, Tokyo, Japan, June 2-5, 1987, pp. 838-842.

44. R. T. Howe, Resonant Microsensors, Technical Digest, *4th International Conference on Solid-State Sensors and Actuators*, Tokyo, Japan, June 2-5, 1987, pp. 843-848.

45. J.C. Greenwood Etched Silicon Vibrating Sensor, *Journal of Physics Engineering & Science Institution*, 17, pp. 650-652.

46. H. C. Nathanson, W. E. Newell, R. A. Wickstrom, and j. R. Davis, Jr., The Resonant Gate Transistor, *IEEE Transistor Electron Devices,* volume ED-14, pp. 117-133.

47. K. E. Petersen and C. R. Guarnieri, Young's Modulus Measurements of Thin Films Using Micromechanics, *Journal of Applied Physics*, Volume. 50, pp. 6761-6766.

48. K. Ikeda, H. Kuwayama, T. Kobayashi, T. Watanabe, T. Nishikawa, and T. Yoshida, Silicon Pressure Sensor with Resonant Strain Gauges Built into Diaphragm, *Technical Digest, 7th Sensor Symposium*, Tokyo, Japan, May 30-31, 1988, pp. 55-58.

49. W. Wang, Z. Yao, J.C. Chen, and J. Fang, Composite Elastic Magnet Films with Hard Magnetic Feature, *Journal of Micromechanical & Microenineering* 14, 1321-1327.

50. R. L. Weber, K.V. Manning, M.W. White and G.A. Weygand, *College Physics*, New York: McGraw-Hill, Chapter 39.

51. Meissner H P and Michaels A S, Surface Tensions of Pure Liquids and Liquid Mixtures *Industrial and Engineering Chemistry* 41 2782.

52. Pennycuick C J, Gliding Flight of the White-Backed Vulture Gyps Africanus, *Journal of Experimental Biology* 55 13.

53. Tupper E C 2004 *Introduction to Naval Architecture 4th edn* (Oxford: Butterworth Heinemann) (Section 9).

54. *Principles of Naval Architecture*, Editor: Comstock J C, Published by *Society of Naval Architects and Marine Engineers*, New York, 1967, pp. 301-311.

55. *Principles of Ships* (Part I), Editors: Sheng Z B and Liu Y Z, Publishers of Shanghai Jiao Tong University, Shanghai, China, 2003, pp. 293-301 (in Chinese)

56. Anthony J. Bianculli, Trains and Technology, *the American Railroad in the Nineteenth Century*, Volumes 1-4, Associated University Presses.

57. Gere J. M., Mechanics of Materials 6th edn Brooks/Cole-Thomson Learning, Belmont, CA.

58. Luo C, Meng F, and Francis A., A New Molding Process to Fabricate Silicon Reinforced PDMS Masters, *Microelectronics Journal 37 1036.*

59. Luo C, Qiao L, Li H., Dramatic Squat and Trim Phenomena of Mm-scaled SU-8 Boats Induced by Marangoni Effect, *Microfluid Nanofluid*, ,Volume 9, Issue 2 (2010), Page 573.

60. Constantine T, On the Movement of Ships in Restricted Waterways. *J Fluid Mechanics*, 9:247–256.

61. D and IW, Ferguson AM, The Squat of Full Ships in Shallow Water. *Trans R Inst Naval Archit* 15:237–255.

62. Millward A, Bevan MG. The Behavior of High Speed Ship Forms When Operating in Water Restricted by A Solid Boundary*, Trans R Inst Naval Archit* 128:189–204.

63. Schofield RB, Martin LA, Movement of Ships in Restricted Navigation Channels. *Proc Inst Civil Eng* 2 85:105.

64. Varyani KS, Squat Effects on High Speed Craft in Restricted Waterways. *Ocean Eng* 33:365–381.

65. E.L. Cussler, Diffusion, Mass Transfer in Fluid Systems, Cambridge university press, 1984.

66. Nicholas Cumpsty, Jet Propulsion: A Simple Guide to the Aerodynamic and Thermodynamic Design and Performance of Jet Engines, Second edition, 2003.

67. W. Johnson, P.D. Soden and E.R. Trueman, A study in jet propulsion: an analysis of the motion of the squid, Loligo Vulgaris*, J. Exp. Biol.* (1972), 56, 155-165.

68. Andrew Packard, Jet Propulsion and the Giant Fibre Response of Loligo, *Nature* 221, 875 - 877 (1969).

69. Suciu, D. G.; Smigelschi, O.; Ruckenstein, *E. AIChE J.* 1967, 13, 1120.

70. Suciu, D. G.; Smigelschi, O.; Ruckenstein, *E. AIChE J.* 1969, 15, 686.

71. Suciu, D. G.; Smigelschi, O.; Ruckenstein, *E. J. Colloid Interface Sci.* 1970, 33, 520.

72. Vazquez, G.; Alvarez, E.; Navaza, J. M. *J. Chem. Eng. Data* 1995, 40, 611.

73. Thomson, J. *Philos. Mag.* 1855, 10, 330.

BIOGRAPHICAL INFORMATION

Mr. Hao Li obtained his B.S. in Electrical engineering specialized in Automatic Control at Huazhong University of Science and Technology (Wuhan, China) in 1998. He was in a PhD program at Louisiana Tech University from 2005 to 2007. After that he transferred to the University of Texas at Arlington to continue his PhD studies. Throughout the years, he has worked on several projects, including fabrication of silicon nanowires, development of SU-8 and PDMS miniaturized boats and flotillas, study of squat and trim phenomena, and gurgling-like effect.